

Chapter 14

Ultrasensitive Xenon MRI and Molecular Imaging

Qingbin Zeng, Yuqi Yang, Lili Ren, Haidong Li, Xiuchao Zhao, Xia Kong, He Deng, Qianni Guo, Shizhen Chen, Xianping Sun, Maili Liu, Chaohui Ye, Xin Zhou*

State Key Laboratory of Magnetic Resonance and Atomic and Molecular Physics, National Center for Magnetic Resonance in Wuhan, Wuhan Institute of Physics and Mathematics, Chinese Academy of Sciences, Wuhan, 430071, P. R. China.

*Corresponce should be sent to: xinzhou@wipm.ac.cn

Nuclear magnetic resonance (NMR) as a powerful tool has been widely used in many fields, such as clinical diagnosis and analytical chemistry. However, the sensitivity of conventional NMR is too low. The sensitivity of NMR promotion is a very important challenge. Spin-exchange optical pumping (SEOP) is a charming strategy to improve the sensitivity of NMR. Our group have increased the sensitivity of noble gases xenon (more than 50,000 folds) via SEOP, and made the noble gas pulmonary magnetic resonance imaging (MRI) came true in China. We have not only obtained the pulmonary ventilation imaging, but also got the pulmonary microstructure parameters by hyperpolarized ^{129}Xe pulmonary MRI to broaden the application fields of hyperpolarized ^{129}Xe . However, ^{129}Xe cannot specifically interact with target. In order to recognize target specifically and improve the detection sensitivity of hyperpolarized ^{129}Xe additionally, we have developed a series of HP ^{129}Xe probes based on cryptophane-A. These probes can detect metal ions, hydrothion, and biothiols specificity and high sensitivity. On the other hand, we have also developed a serious of microenvironment stimulated probes to decrease

the background noise and increase the sensitivity for targeted cancer cell detection and treatment. Last but not least, we have developed ultra-low field spectrometer based on magneto-optical rotation to determination of magnetic nanoparticles, which have broadened the application fields of NMR.

14.1 Ultrasensitive pulmonary gas magnetic resonance imaging

14.1.1 Background

Magnetic resonance imaging (MRI) is a non-invasive and non-ionizing radiation imaging method, and has been widely used in clinical diagnosis. Due to the specific advantages (such as high resolution, high depth of tissue penetration, superior soft tissue contrast, and multi-parameter imaging), MRI is widely applied in clinical medicine for diagnosis of diseases. However, MRI has great challenges in detection of lung diseases because the lung has a typical cavity structure (the ^1H density in the lung is 1000 times lower than that of the normal tissue). Therefore, the lung is a “blind zone” for traditional MRI, and the structure or function information of the lung is difficult to detect. Recently, in the research using hyperpolarized (HP) gas, pulmonary MR images can be acquired when the HP noble gas is inhaled by volunteers. This enables the noninvasive detection of lung diseases, providing a new idea for pulmonary MRI^[1-3].

Xenon is a non-toxic and harmless noble gas, which is very suitable for biomedical applications^[1,3,4]. Spin-exchange optical pumping (SEOP) can be used to enhance the nuclear spin polarizations of noble gases (more than 10000 folds) ^[5,6], which makes HP noble gas lung MRI feasible. According to the theory of SEOP (as shown in Figure 14.1)^[5,7-9], we designed and constructed an experimental device for HP ^{129}Xe gas generation based on the computer control (viz., HP noble gas generation device, which can achieve 50,000-fold increase in the nuclear spin polarization of xenon^[10]). By transmitting the HP ^{129}Xe gas into the lung, pulmonary ventilation function is visualized. In addition, the gas-gas and/or gas-blood exchange dynamics of HP ^{129}Xe can be measured by utilizing the difference of solubility and chemical shift of xenon in lung tissue and blood. In this way, the quantitative and visual measurement of the exchange function in the lung can be achieved.

Since the nuclear spin polarization of HP gas is unrecoverable, the mechanism of the radio frequency (RF) excitation will have important influence on the image quality of pulmonary ventilation MRI. Conventional RF excitation includes the constant-flip-angle (CFA) and variable-flip-angle (VFA) strategies. When the MRI data acquisition begins at the k-domain center, the CFA results in an image of high SNR but sacrifices the accuracy of spatial information. On the other hand, the VFA results in high accuracy but suffers from a low SNR. Therefore, we proposed a novel scheme, called constant-variable flip angles (CVFA), to optimize both the SNR and accuracy. In this way, the CVFA not only fully utilizes the polarization of ^{129}Xe , but also acquires the image with high signal-to-noise ratio (SNR) and high resolution^[11].

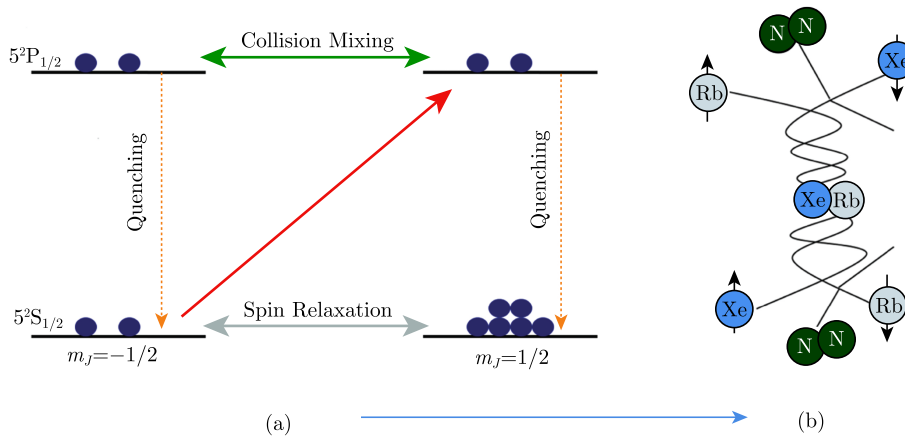


Figure 14.1 The diagram of SEOP. The process of SEOP can be divided into two steps: (a) The angular momentum of laser photons is transferred to Rb, making the outer valence electron of Rb atom polarized (i.e., laser pumping). (b) the ^{129}Xe atom collided with the highly polarized alkali metal. Then the angular momentum of the Rb electrons is shifted to the ^{129}Xe nucleus, achieving the spin polarization of the ^{129}Xe nucleus (i.e., the spin exchange process).

14.1.2 Lung ventilation imaging

After determining the power, angle and excitation mechanism of the RF sequence, we can perform the lung ventilation imaging and obtain the ventilation distribution image using HP technique^[12]. This can acquire the local ventilation feature image of the lung. The obstruction of ventilation is the manifestations in lots of lung diseases (such as the radiation-induced lung injury (RILI) and lung tumor). The

ventilatory status of the lungs can be obtained by analyzing the lung ventilation images, which is helpful to determine the location of the airway obstruction and the pulmonary parenchyma changes. In addition, it can be used as a grading standard for some diseases (such as COPD). In the lung ventilation imaging with HP gas, 2D and/or 3D images are acquired by using small angle damage gradient echo imaging technique with short echo time when the HP gas is inhaled. Figure 14.2 and Figure 14.3 show the lung ventilation defects in the ventilation images of healthy volunteers and patients. Due to the presence of narrow or blocked bronchi in patients with COPD, there is little HP ^{129}Xe in the respiratory bronchial segment, leading to the obvious low signal and lack of signal.

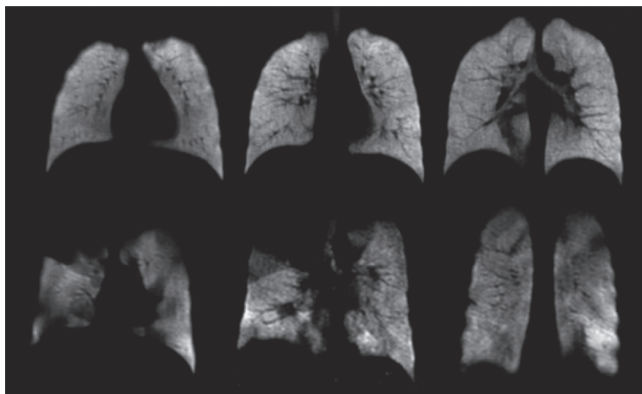


Figure 14.2 HP ^{129}Xe pulmonary ventilation images in normal volunteers (upper) and patients with COPD (below).

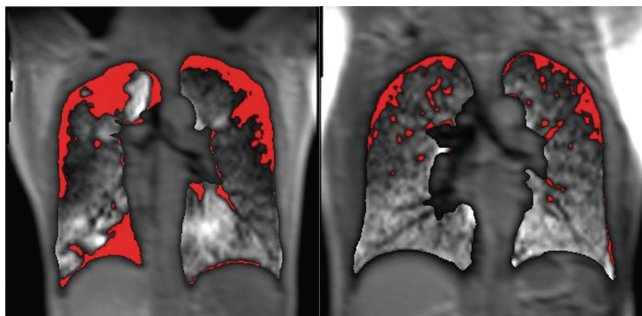


Figure 14.3 Ventilation images and ventilation defects in patients with COPD and healthy volunteers. The red color denotes the region with ventilation defects. In the left figure, the ventilation defect percentage (VDP) = 22.06%. As for the right figure, the VDP = 7.58%.

14.1.3 Lung microstructure and function

The diffusion of gas in the lung is related to the microstructure of the lung, so the change of the microstructure of the lung will affect the diffusion characteristics of HP gas. Therefore, the measurement of the HP gas diffusion in the lung can be used to detect the change of lung microstructure with high sensitivity (e.g. HP gas diffusion MRI). The distribution and mean value of apparent diffusion coefficients (ADCs) of HP gas in the lung can be derived through the simplified Gaussian diffusion model^[13]. In HP ^{129}Xe diffusion MRI with single b -value, gas diffusion coefficient is measured to depict the change of lung microstructure. Although this can reflect the changes of lung microstructure to some extent, it is an indirect method and only one parameter (ADC) is acquired. Meanwhile, due to the complexity of pulmonary microstructure, the diffusion of HP ^{129}Xe in the lung is not pure Gauss type diffusion in the diffusion imaging with multi b values. Therefore, the quantitative measurement of lung microstructure by multi b diffusion imaging with HP ^{129}Xe is an important method for lung noninvasive visualization and early diagnosis of lung diseases. According to the simplified pulmonary gas-blood exchange model, we can quantitatively measure the pulmonary microstructure parameters of model rats with emphysema by HP ^{129}Xe multi b value diffusion MRI. In this way, the distribution of parameters (such as the pulmonary airway diameter (R), airway diameter (R), alveolar depth (H), alveolar surface volume ratio (S/V) in the lungs) can be obtained effectively and reasonably^[14].

HP gas diffusion MRI has been demonstrated to be sensitive to changes in lung microstructure. Since the lung microstructure is very complex and the gas diffusion is faster than the solid and liquid, the diffusion of HP gas in the lung will deviate from the single exponential decay with the increase of the b value, which means the diffusion of HP gas in the lung is non-Gaussian type diffusion. Diffusion kurtosis imaging (DKI) is a method based on the proton MRI diffusion method for describing the non-Gaussian type of proton diffusion. Experimental results show that the HP ^{129}Xe has a strong correlation with lung microstructure, and DKI is very suitable for describing the non-Gaussian type diffusion of HP ^{129}Xe in the lung^[15].

In addition to detecting the lung microstructure with diffusion imaging, HP ^{129}Xe MRI can study the gas-blood exchange function of lung by using chemical shift saturation recovery (CSSR). The good lipid solubility and chemical shift sen-

sitivity of HP ^{129}Xe enables the direct measurement of HP ^{129}Xe signals in lung tissues and blood. The dynamic spectra of HP ^{129}Xe in tissues and blood with the variation ratio of HP ^{129}Xe signal in blood and tissues can be obtained by using the dynamic spectra measurement. Then, the variation ratio of HP ^{129}Xe signal in tissues and blood reflects the changes of lung tissue and lung perfusion. With the dynamic spectra of pulmonary HP ^{129}Xe combined lung gas exchange model, we can quantitatively obtain the physiological parameters (such as lung gas-blood exchange function and lung structure), which cannot be measured in a noninvasive way by any other methods at present. Thus, we quantitatively investigated and evaluated the pulmonary gas-blood exchange function of the lung with RILI or COPD using HP ^{129}Xe MRS and MRI^[17].

In HP ^{129}Xe MRI measurements, diffusion weighted imaging (DWI) provides valuable information for assessing the morphological parameters of the lung, and the CSSR technique can assess the gas-blood exchange function. In previous works, these two techniques can only be performed in separately breath. However, multiple breathing increases the cost and scanning time of HP gas MRI, limiting the clinical application. Moreover, due to the inconsistent physiological state of the lung, different breath holding procedures will increase the measurement error. To solve this problem, we propose a new method (called diffusion weighted chemical shift saturation recovery (DWCSSR)) to integrate the DWI and CSSR data acquisition in a single breath-hold. Compared with the continuous breathing schemes (i.e. CSSR+ DWI and DWI + CSSR), the DWCSSR scheme can significantly shorten the breath-hold time and obtain higher SNR. This suggests that the proposed method can obtain comprehensive information about the lung structure and function in one breath-hold. The *in vivo* experimental results demonstrate that DWCSSR has great potential for the evaluation and diagnosis of lung diseases^[18].

Due to the limitations of imaging devices, medical images are undoubtedly degraded by different types of noise, blurred or other degradation. Fuzzy set methods, based on nonlinear knowledge, can process imperfect data derived from vagueness and ambiguity. We presented a new enhancement method based on intuitionistic fuzzy sets^[19,20], which can separate normal and pathological regions effectively in HP ^{129}Xe MRI, then obtain structure and function information of lung. This is useful for detecting functional and structural changes in pulmonary diseases.

The dynamic visualization of lung ventilation process is able to provide compre-

hensive information of pulmonary structure and function. This information is not only helpful to estimate the gas flow patterns in the trachea, the gas flow velocity and direction in the whole lung, and the airway resistance, but also useful to understand and evaluate the lung diseases. Therefore, with the combination of compressed sensing (CS), a novel method of HP gas dynamic MRI based on the variable sampling rate is proposed. Figure 14.4 shows the 15 frames of HP ^{129}Xe inspiratory dynamic MR images of a healthy volunteer (1.5 Tesla whole-body MRI Scanner, Avanto, Siemens Medical Solutions. The polarization of xenon is approximately 20%).

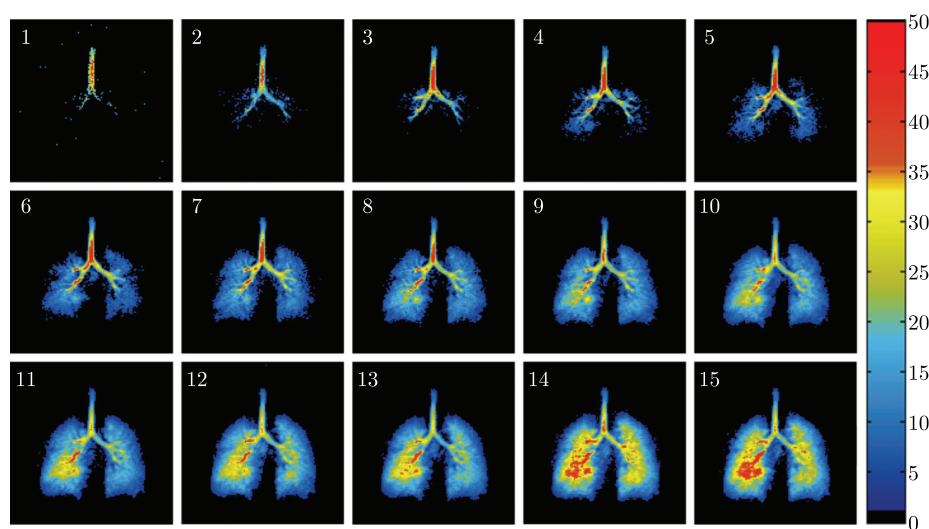


Figure 14.4 Lung inspiration process imaging based on HP ^{129}Xe MRI^[21]

With the SEOP technique, the signal of ^{129}Xe gas can be greatly improved and HP gas MRI can be achieved. Combined with the specific pulse sequence, we can detect the physiological parameters of lung microstructure and the gas-blood exchange function in a single breath-hold. In this way, we can further study the early diagnosis of lung diseases and related pathology, which is promising to be applied in clinical diagnosis and treatment in the near future.

14.2 Ultrasensitive HP ^{129}Xe NMR probes

^{129}Xe is a nontoxic and inert gas, and the chemical shift of which is extremely susceptible to the surrounding environment. Most importantly, ^{129}Xe has no background signal in biological tissue. As a result, it is especially suitable for biomedical

applications. While hyperpolarize ^{129}Xe by SEOP, the signal intensity of HP ^{129}Xe is 50,000-fold larger than thermal polarized one. Thus, the HP ^{129}Xe has potential application in MRI of lung and brain *in vivo*.

But ^{129}Xe can nonspecifically interact with proteins, lipids, spores, and cryptophanes. So, using the HP ^{129}Xe as probe directly is hard to recognize target specifically at molecular level. In order to overcome the shortage, Spence M. and co-workers provide a new strategy to construct HP ^{129}Xe biosensor^[22]. They choose cryptophane-A as the host molecule of ^{129}Xe , and use biotin to functionalize the cryptophane-A cage. While the functionalized cryptophane-A specific interaction with avidin, it will affect the electron density experienced by the encapsulated ^{129}Xe , resulting in the change of chemical shift (Figure 14.5). The functionalized cryptophane-A has endowed the HP ^{129}Xe with specificity. The cryptophane-A cage provides most suitable xenon affinity ($4,000 \text{ M}^{-1}$, in organic solvent) and exchange kinetics (the residence time range is 30~300 ms, in aqueous solution) among all the cryptophanes, making it an excellent host for xenon atoms.

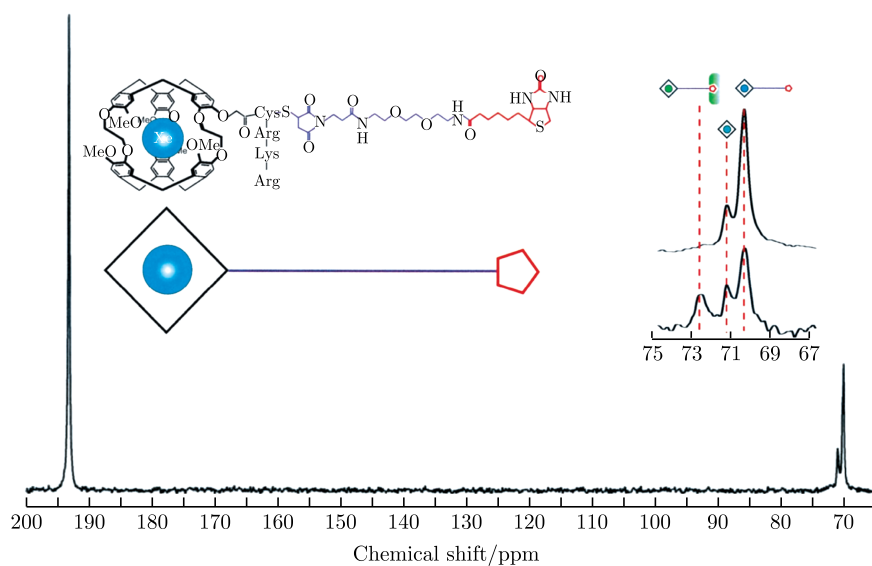


Figure 14.5 Structure of HP ^{129}Xe biosensor based on cryptophane-A, and the HP ^{129}Xe NMR spectra obtained in the presence of avidin. (Figure was adapted with permission from Ref [22], copyright © 2001, The National Academy of Sciences)

In order to improve the detection sensitivity, a method called Hyper-CEST was

reported in 2006^[23]. Hyper-CEST is a technique which combined the hyperpolarization technique with the chemical exchange saturation transfer (CEST) detection method. In this method, saturated rf pulses were used to saturate the bound signal in cryptophane-A selectively. On account of the xenon exchange between the cage and solution, the depolarization resulted in a signal loss of the dissolved ^{129}Xe (^{129}Xe @ solution), which could be easily detected (Figure 14.6). This method improves the sensitivity of the xenon biosensor by orders of magnitude, reaching sensitivity levels of molecular imaging.

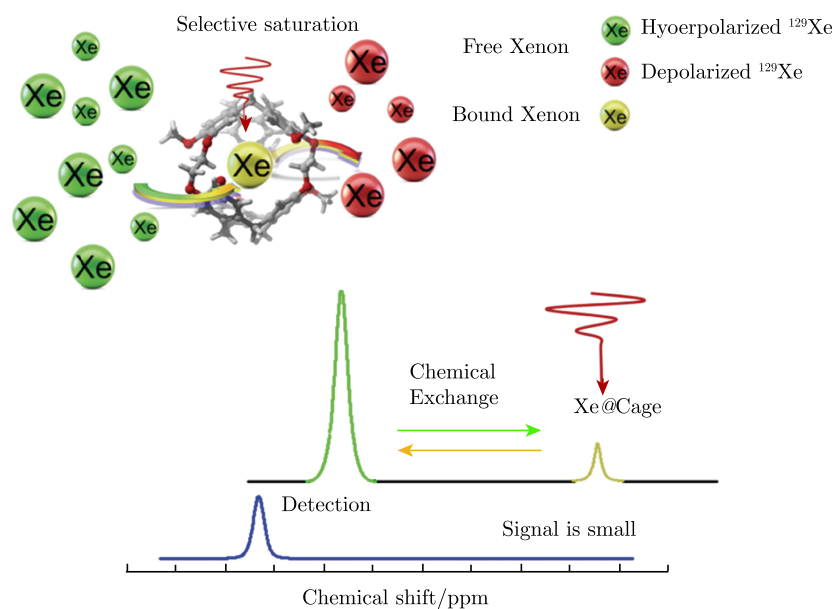


Figure 14.6 Hyper-CEST detection scheme for ^{129}Xe in the cryptophane-A cage. Initial spectrum (colorful line) and resulting spectrum (blue line) from selective saturation of the caged ^{129}Xe (^{129}Xe @ cage) and proportionate bulk dissolved ^{129}Xe @ solution depolarization.

In recent years, a wide range of ^{129}Xe biosensors based on cryptophane-A have been developed. Our laboratory have developed a series of HP ^{129}Xe probes based on cryptophane-A to detect metal ions^[24,25], hydrothion^[26], and biothiols ^[27,28]in cells.

14.2.1 HP ^{129}Xe probe for metal ions

Zinc is an essential trace element in the human body and is the second most

abundant transition metal in the living organisms. Zn^{2+} not only constitutes many enzymes and proteins, but also plays a key role in various physiological processes. Either a deficiency or excess of Zn^{2+} will cause a physiological dysfunction of the organism^[29]. Thus, it is of great significance to develop a highly sensitive and specific method for the detection of Zn^{2+} . Nowadays, the noninvasive methods to monitor the distribution of Zn^{2+} in different tissues in body are optical imaging and magnetic resonance imaging. However, optical methods suffer from limited penetration depth. On the other hand, conventional MRI techniques suffer from reduced sensitivity and often lack selectivity. Therefore, to develop more sensitive and more selective method is crucial importance.

Our group have developed a new HP ^{129}Xe probe, which shows high selectivity for Zn^{2+} ^[24]. This probe was combined by cryptophane-A and 2-(diphenylphosphino) benzenamine, and the 2-(diphenylphosphino) benzenamine as ligand for Zn^{2+} . This probe shows good selectivity for Zn^{2+} , while the probe exposure to Zn^{2+} , the chemical shift of encapsulated ^{129}Xe changed 6.4ppm to upfield, which was nearly four times larger than that of the reported similar probe.

As we known, mercury pollution remains a problem of global proportions perpetuated by the occurrence of natural geological events and the widespread use of mercury species in human activities. Fluorescence-based sensors do not provide depth resolution needed to image spatial distributions. So, our group had developed another metal ions sensitive HP ^{129}Xe probe, which have high selectivity for Hg^{2+} ^[25].

This probe was combined by a dipyrrolylquinoxaline (DPQ) derivatives and two cryptophane-A cages. The DPQ derivatives act as cation receptors, whereas cryptophane-A act as a host molecular for xenon. This probe like a molecular clamp, which can clip the target ions in its clamp's cave, using DPQ as the basic molecular frame, pyrrole and the imine as the recognition site, and cryptophane-A as the HP ^{129}Xe NMR signal reporter moiety.

While the probe exposure to Hg^{2+} , the chemical shift of ^{129}Xe in cryptophane cage changed 38.6 Hz to upfield. When using Mg^{2+} , Ca^{2+} , Zn^{2+} , and Cd^{2+} instead of Hg^{2+} , no obvious change in the signal of ^{129}Xe caged in cryptophane could be observed. Compared with other HP ^{129}Xe based sensors of metal ions, the downfield change of chemical shift caused by electron-withdrawal effect of metal ions, the upfield change of chemical shift of ^{129}Xe in cryptophane cage of our probe was

totally different. Since design of this probe is totally different from our previous designed probe, the change of chemical shift of $^{129}\text{Xe}@$ cryptophane is influenced not only by the electron-withdrawing effect of the metal ions, but also by the shielding effect of the two cryptophane-A cages. This result not only demonstrate that the Hg^{2+} ions were indeed chelated with the DPQ moiety, but also suggest that the distance between the two cryptophane-A cages of probe is reduced after binding. When binding with Hg^{2+} the molecular structure of probe turned from open to closed (Figure 14.7(b)). As the electron clouds of the two cryptophane-A cages overlap, the shielding effect towards encapsulated ^{129}Xe becomes important. The influence of shielding effects from electronic clouds of the two cryptophane-A cages

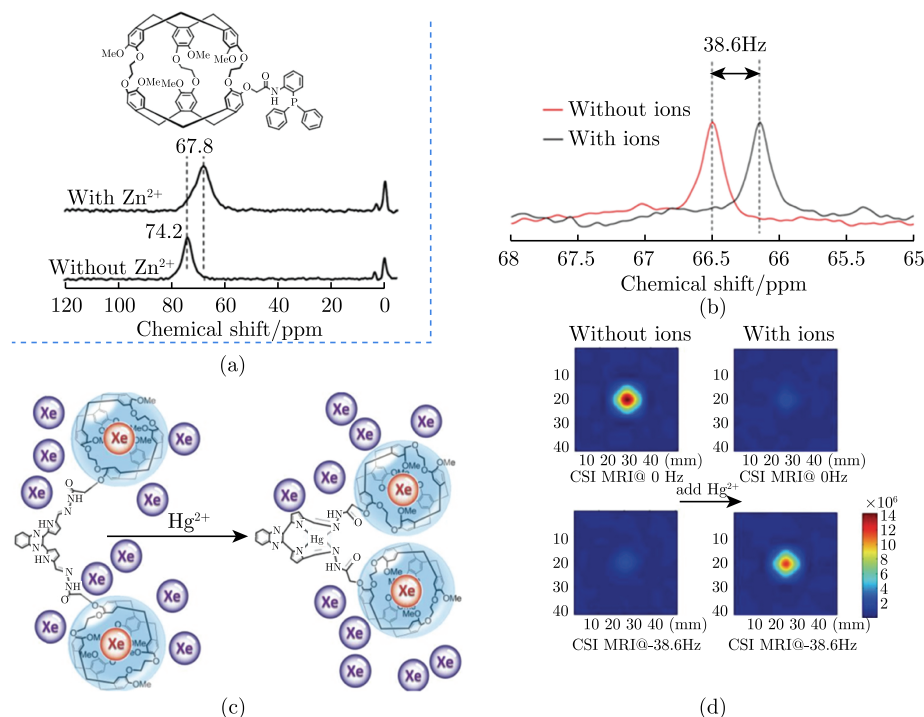


Figure 14.7 (a) HP ^{129}Xe NMR spectra obtained for probe in the presence and absence of Zn^{2+} . Figure was adapted with permission from Ref [24], copyright © 2014 Elsevier B.V. (b) Conformational change of probe induced by its interaction with Hg^{2+} . (c) HP ^{129}Xe NMR spectra obtained for probe in the presence and absence of Hg^{2+} . (d) Chemical shift image (CSI MRI) of probe with, and without the addition of Hg^{2+} . (Figure was adapted with permission from Ref [25], copyright © 2016 WILEY-VCH Verlag GmbH & Co. KGaA, Weinheim)

overlapping was stronger than the deshielding effect of the electron-withdrawal effect of metal ions on the chemical shift of ^{129}Xe in cage, an upfield change of chemical shift of $^{129}\text{Xe}@cage$ was induced.

The change in chemical shift between the signals of encapsulated xenon in the absence and in the presence of Hg^{2+} ions relative to the NMR linewidths was sufficient to enable spectroscopic MRI of these chemical species. Figure 14.7(d) images were obtained using a CSI method. Comparison between images without and with Hg^{2+} in Figure 14.7(d) shows that the Hg^{2+} ions can be specifically detected and localized at low concentration in a short time.

14.2.2 HP ^{129}Xe probe for hydrothion

Hydrogen sulfide (H_2S), traditionally known for its characteristic offensive odor and toxicity, has recently been shown to be a significant gaseous signaling transmitter in living organisms. The involvement of endogenous H_2S has been demonstrated in several physiological and pathological processes, such as regulation of cell growth, cardiovascular protection, modulation of neurotransmission, and anti-inflammation action. Moreover, recent studies have shown that any imbalance H_2S levels can lead to health problems, including the symptoms of Alzheimer's disease, Down's syndrome, and diabetes^[30].

Continuing our interest in developing HP xenon based probes, we developed a new ^{129}Xe MRI probe for H_2S detection based on a H_2S -specific response reaction (Figure 14.8(a))^[26]. To investigate the feasibility of this design concept, we chose cryptophane-A as a host for ^{129}Xe and a known H_2S mediated specific response group as the reaction site. An azido reduction reaction can selectively detect H_2S , because the azide group can be easily converted into amine upon reaction with H_2S .

As designed, probe was found to be weakly fluorescent (Figure 14.8(b)). After addition of HS^- to the solution of probe, a strong green fluorescence was observed. Fluorescence spectra show the intensity at 534nm gradually increased along with the time until it reaches emission saturation (about 25-fold) within 10min (Figure 14.8(b)). These results suggest that probe shows fast response towards H_2S .

Encouraged by the above results, the application of probe in HP ^{129}Xe NMR spectroscopy was evaluated. Under the same test conditions, the ^{129}Xe NMR signal of encapsulated xenon in probe at 75.2ppm. Notably, a new signal at 74.1ppm emerges and meanwhile the signal at 75.2ppm disappears after the addition of HS^- .

Evidently, a chemical shift change of 1.1 ppm between the signals of caged xenon in the absence and presence of HS^- was observed (Figure 14.8(c)). These results reveal that the response of probe towards HS^- leads to a chemical structure transformation that can be detected and differentiated by HP ^{129}Xe NMR spectroscopy.

Most importantly, both the fluorescence imaging and hyper-CEST NMR/MRI have demonstrated that although in live cells, this probe can make good response to H_2S (Figure 14.8(d), (e), (f)).

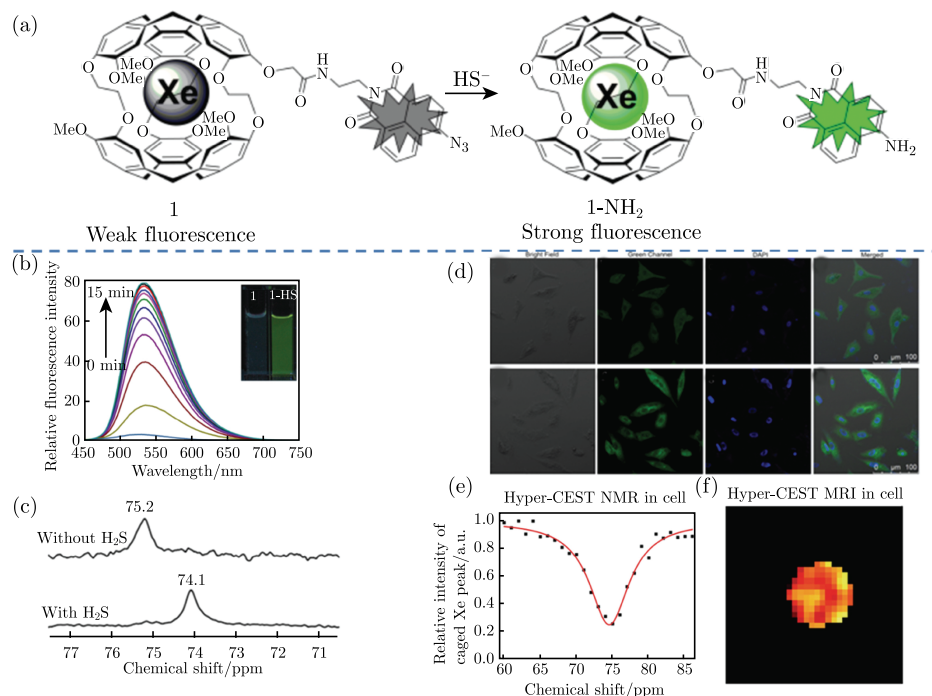


Figure 14.8 (a) Schematic of HP ^{129}Xe sensor for H_2S detection. (b) Fluorescence spectrum of probe upon addition of HS^- in HEPES buffer solution. (c) ^{129}Xe NMR spectra change of probe upon addition of HS^- in HEPES buffer solution. (d) Fluorescence images of H_2S using probe in A549 cells. (e) Hyper-CEST spectra of probe-labeled A549 cells. (f) Hyper-CEST MRI of probe in cells. The Hyper-CEST effect was calculated by using the formula $\text{CEST effect} = (\text{off}_{\text{Res}} @ \text{on}_{\text{Res}}) / \text{off}_{\text{Res}}$. (Figure was adapted with permission from Ref [26], copyright © 2017 Wiley-VCH Verlag GmbH & Co. KGaA, Weinheim)

14.2.3 HP ^{129}Xe probe for biothiols

Biothiols play important roles in cell growth, apoptosis inhibition, DNA synthe-

sis, and angiogenesis. Abnormal biothiol levels in cells are directly correlated to the occurrence of cancer, Alzheimer's disease, Parkinson's disease, and cardiovascular disease^[31,32]. Thus, it would be desirable and perhaps critically important to develop methods to detect biothiols in living systems.

During the past decades, considerable efforts have been devoted to developing various methods for biothiol detection *in vitro*. Fluorescence spectroscopy compared to other techniques have some significant advantages, such as high sensitivity, simplicity, and non-invasive detection, make it become one of the most popular methods for biothiols detection. Unfortunately, the main drawback of fluorescence method is poor penetration depth due to light scattering in optically opaque media. This disadvantage makes fluorescence methods less suitable for imaging tissue. Magnetic resonance imaging (MRI), which is a powerful tool for the early detection of disease, features high spatial resolution and deep tissue penetration. Unfortunately, ¹H MRI was found to lack the sensitivity required to detect physiologically relevant changes in biothiols levels. HP NMR is a good method, which not only have ultrahigh sensitivity, but also have these advantages of NMR.

In order to realize high sensitive detection of biothiols, we designed a HP ¹²⁹Xe probe, which can detect biothiols via HP¹²⁹Xe NMR^[27]. The probe incorporates two parts: cryptophane cage conjugated to a ligand possessing an acrylate group. Cryptophane acts as a host for the capture of xenon atoms and alters the ¹²⁹Xe NMR chemical shift based on binding to the ligand (Figure 14.9(a)). The acrylate group, which is known to be involved in thiol-addition reactions to generate thioether, was selected to react with biothiols.

While the probe exposure to 3 equiv Cys, notably, a new signal appears at 75.5ppm, which changed 1.4ppm to upfield compared to the probe in solution. This new resonance is attributed to probe undergoing a thiol addition reaction with Cys to produce a new cryptophane derivative. By recording ¹²⁹Xe NMR spectra as a function of time, the intensity of the signal at 76.9ppm gradually decreases in about 30min. Concomitantly, the integral intensity of the new signal at 75.5ppm increases until it reaches a saturation (Figure 14.9(b)).

After addition of Hcy and GSH respectively, a similar ¹²⁹Xe NMR spectral response was observed (Figure 14.9(c), (d)). This suggests that the reaction of probe with Hcy or GSH also experience a similar reaction as Cys. The new emerging signal appears at $\delta = 75.7$ ppm and is associated with an increase of 1.2ppm (upfield) in

the chemical shift. By contrast, the integral intensity of the signal at $\delta = 76.9\text{ppm}$ for Hcy and GSH takes more than 3 h to disappear. That means the thiol-addition reaction rates of probe with Hcy (pKa: 8.87) and GSH (pKa: 9.20) are much slower than that of Cys (pKa: 8.30), which may be ascribed to their different pKa values. The above results demonstrate that probe not only can monitor biothiols levels through ^{129}Xe NMR, but also can discriminate Cys over Hcy and GSH through chemical shift and average reaction rate.

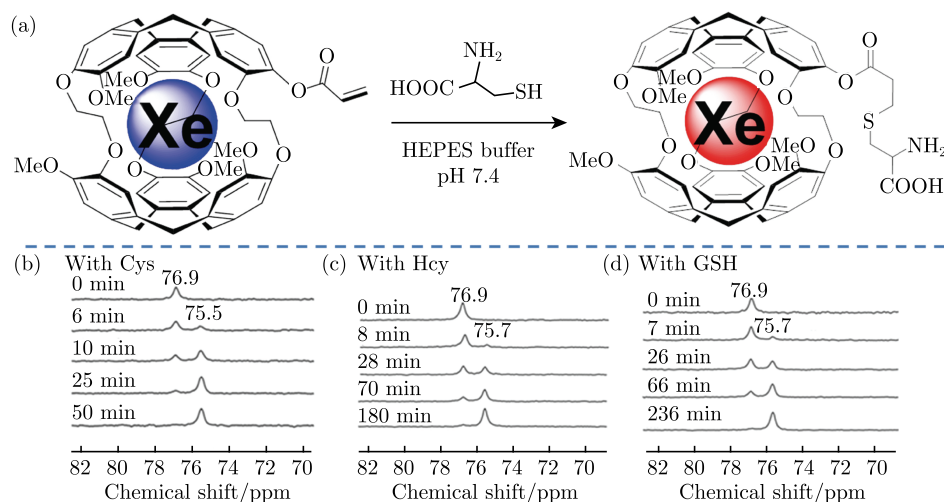


Figure 14.9 (a) Proposed reaction mechanism of probe with Cys. (b), (c), (d) Time-dependent ^{129}Xe NMR spectra change of probe upon addition of 3 equiv Cys, Hcy, GSH. (Figure was adapted with permission from Ref [27], copyright © 2016, American Chemical Society)

This probe shows high selectivity for biothiols, however, the probe cannot detect biothiols in cells. In order to realize detect biothiols in cells, our group developed another HP ^{129}Xe probe, which can be used to detect biothiols in cells via fluorescence/ ^{129}Xe -NMR^[28].

This new probe composed of a host molecule (cryptophane-A), a disulfide-linker (linker), a fluorescence moiety (naphthalimide), and a targeting group (triphenylphosphonium). While the probe exposure to GSH, the fluorescence intensity at 560nm was enhanced 11-fold (Figure 14.10(c)) while the fluorescence changed from blue to green-yellow. Through introduce an electron-withdrawing carbamate group to convert the 4-amino donor into a weak donor, the ICT effect of the fluorophore is

weakened to result in a blue shift of fluorescence. While the probe underwent biotriols, the disulfide bond cleaved followed by intramolecular cyclization and cleavage of a neighboring carbamate bond to release aminonaphthalimide moiety and leads to the fluorescence changes. These results demonstrate that the signal from the cryptophane-A probe is modulated by GSH.

To investigate how GSH can be monitored by ^{129}Xe NMR, ^{129}Xe NMR spectra of probe were acquired. The GSH concentration dependence ^{129}Xe NMR spectra are shown in Figure 14.10(d). When the concentration of GSH is increased, the xenon signal intensity at 70.1ppm increases, whereas that at 71.5ppm decreases. This demonstrates that probe reacts with GSH. The addition of GSH resulted in the chemical shift of caged Xe (Xe@ cryptophane-A) to shift by 1.4ppm in the upfield direction. The Xe@cryptophane-A signal did not show further changes when the concentration of GSH reached 1.25mM (50 equiv). This trend was consistent with the fluorescence spectra. This probe have high sensitivity, 1 μM probe can produce 20% CEST effect, which is still at least 3~4 orders of magnitude more sensitive than ^1H CEST contrast agents. And the detection threshold of this probe is 200pM. This low detection threshold implies that this probe and ^{129}Xe NMR have the potential for detecting thiols in cells at low concentration.

While in cells, this probe can make good response to biotriols too. As shown in Figure 14.10(e), the cells were treated with N-ethylmaleimide (NEM) followed by the probe, in the presence of the agent the fluorescence intensity of cells treated with probe decreased significantly. These results prove that this probe can be used for biotriols detection in cells. On the other hand, to confirm whether cellular thiols can be monitored by ^{129}Xe NMR, the Hyper-CEST method was investigated in cell studies. After the probe incubation with the cells, only one signal appeared around 73ppm corresponding to ^{129}Xe @ cryptophane-A in cells. While the cells incubated with NEM firstly, and then incubation with the probe, a signal appeared around 73ppm too. But the signal of ^{129}Xe @ cryptophane-A was much smaller than for the experimental group (Figure 14.10(f)). The hyper-CEST spectra was kept consistent with fluorescence images, these results demonstrate that the probe can be used to detect biotriols in cells by Hyper-CEST spectra.

HP ^{129}Xe biosensors not only have ultrahigh sensitivity, but also can be functionalized for different applications. In the future, such biosensors have the potential to detect various diseases, by localizing HP ^{129}Xe to tissues and by providing mul-

tultiplexed detection of different biomarkers.

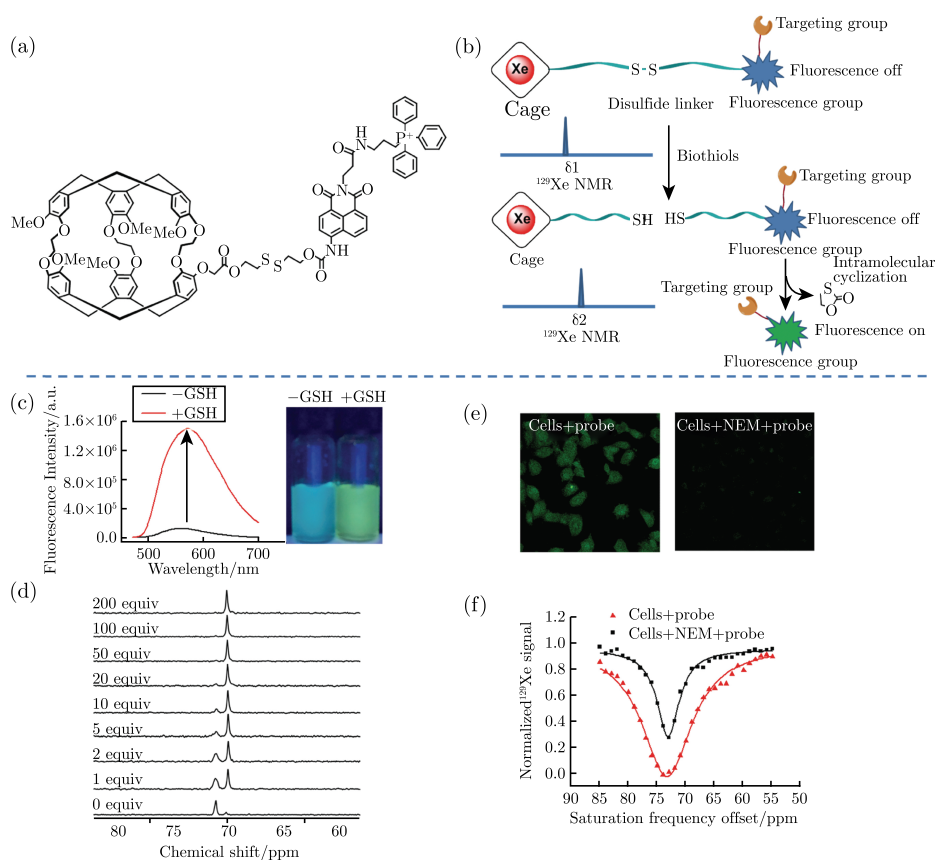


Figure 14.10 (a) Structure of the probe. (b) Proposed reaction mechanism of probe with biothiols. (c) Fluorescence spectra and photos of probe recorded in the presence and absence of GSH. (d) ^{129}Xe NMR spectra (average of 16 scans, line broadening = 10Hz) of probe response to different equivalents of GSH. (e) Fluorescence images of H1299 cells treated by probe and NEM. (f) Hyper-CEST spectra of probe response to biothiols in lung cancer cells (H1299). (Figure was adapted with permission from Ref [28], copyright © 2017, American Chemical Society)

14.3 Microenvironment responsive probes

The balance between cells and surrounding makes proliferation, differentiation and apoptosis progress in a right way. Cancer originates from mutations in genes

that regulate essential pathways of cell function leading to uncontrolled outgrowth of tissue cells. The resulting tumor will form a microenvironment to support the cell immortalization. Latest research shows that the temperature^[33], pH^[34], oxygen^[35], proteins^[36] and metabolite^[37] in tumor area are obviously different from normal tissues. According to these differences, our group developed a series of tumor microenvironment stimulated probe to decrease the background noise and increase the sensitivity for targeted cancer cell detection and treatment.

The high energy production of tumor area leads to higher temperature within normal tissue. Based on this effect, a micelle particle, which morphology changes sharply between 37°C and 40°C, was introduced to detect the tumor cells by monitoring the significant amplification of the chemical exchange saturation transfer (CEST) signal. In this study, a smart micelle was fabricated by two temperature stimulated unimer chains with different length^[38]. The short chain was linked to a Para CEST agent europium (III) tetra amide complex (EuDOTA-4AmCE) via diamine. The different length of amphiphilic chains self-assemble as a core-shell micelle. As shown in Figure 14.11(a), the stretched hydrophilic chains embed the contrast agents when the temperature is below the micelle's lower critical solution temperature (LCST). When the temperature is above LCST, the fold of the long chain would expose the Eu (III) modified short chains to the bulk water, and lead to much stronger CEST signal. By change the ratio of the two chains, we successfully control the LCST of the micelle particle around 37°C (Figure 14.11(b)). Due to the obvious CEST signal change around body temperature, the smart micelle system may be useful for detecting temperature changes under abnormal conditions or during hyperthermia treatment.

It is significant for the research of the formation of atherosclerosis to achieve high-sensitive detection of macrophages. High-density lipoprotein (HDL) is a kind of lipid-protein complex nanoparticles existing in blood vessel, and the main function of HDL is called reverse cholesterol transfer. HDL has specificity to the SR-BI receptor expressed on macrophages. It is commonly considered that the progress of atherosclerosis is related to the formation of foam cells after the macrophages enter the artery wall. Thus, it is significant for the research of the formation of atherosclerosis to achieve high-sensitive detection of macrophages. MRI contrast agents based on reconstituted HDL (rHDL) for the detection of atherosclerosis plaques were developed recently. Paramagnetic chemical exchange saturation transfer (ParaCEST)

is a newly developed magnetic resonance method. Unlike traditional MRI methods, ParaCEST is mainly based on the exchange between the bound water on Ln chelate and bulk water. We have designed and prepared a high-sensitive ParaCEST MR/fluorescence dual-modal contrast agent based on rHDL, Eu-Rhod-rHDL, and ParaCEST sensitivity was enhanced^[39]. The advantage of developing dual-modal contrast agent is the complementarity of ParaCEST and fluorescence. A phospholipid with Eu(III) chelate conjugated on is synthesized, which is ParaCEST active. After the self-assembly process of lipids and proteins, dual-modal rHDL contrast agent is made. In comparison of traditional small molecular ParaCEST agents, the detection sensitivity of Eu-Rhod-rHDL is enhanced by 129 folds, and thus expands the application range of ParaCEST method. Meanwhile, the Eu-Rhod-rHDL is able to target macrophages and enter macrophages specifically. Thus the detection of macrophages was achieved. This dual-modal rHDL also has potential for the ParaCEST detection of atherosclerosis.

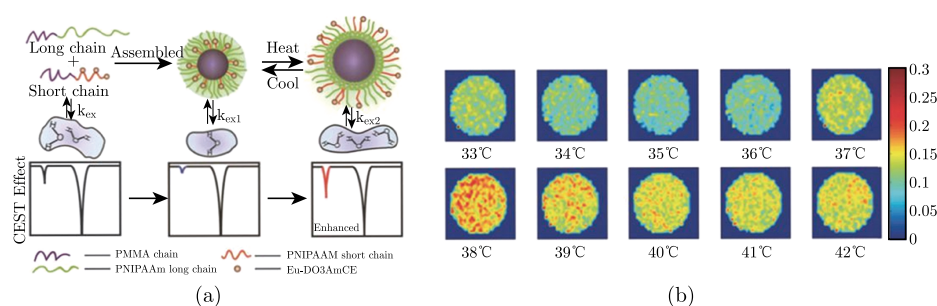


Figure 14.11 (a) A schematic diagram of the CEST MRI signal changes in response to the micelle's morphological changes. The temperature change around the LCST affecting the PNIPAAm chain, which is folded as an aggregated cluster when the temperature is higher than the LCST of 37°C. (b) The CEST MR phantom images at different temperatures obtained using a 9.4T micro-imaging system with a saturation pulse of 8 μ T for 5s. (Figure was adapted with permission from Ref [38], reproduced by permission of The Royal Society of Chemistry)

Certain cells can be detected selectively by above contrast agents. Further, early accurate diagnosis and realtime, safe and effective tumor detection technologies are needed in improvement of cure rate and life quality of the patient. MRI (magnetic resonance imaging) usually needs molecular imaging probes to improve the signal

and image the targeted tumor site. Non-invasive and realtime diagnosis and monitoring of disease therapeutic responses were realized by liposomes simultaneously. Here, a kind of multifunctional liposomal MRI probes was developed for lung cancer detection and therapy, including T_1 contrast agents Gd-DOTA and anti-cancer drug paclitaxel^[40]. Further c(RGDyK) modification could target to tumor in vivo. This targeted liposome greatly enhanced the cytotoxicity of the drug to tumor cells A549 by in vitro MTT studies. The T_1 relaxivity in tumor cells treated with the targeted liposome formulation was increased 16-fold when compared with the non-targeted group. The tumors in mice were clearly visualized using T_1 -weighted imaging after administration of the liposome. Fluorescence images also showed the targeted effect of this liposome in tumor cells. This nanoparticle overcame the insolubility of paclitaxel, reduced the side effects of FDA-approved formulation of PTX-Cre (Taxol[®]) and improved the drug delivery efficiency to the tumor. These findings lay the foundations for the further tumor inhibition studies and application of this delivery vehicle in cancer therapy settings.

Based on the foregoing studies, a theranostic dual drug-loaded liposomal drug delivery system was developed, which integrate multimodality targeted imaging and doublet chemotherapy drug delivery. Platinum-based drugs and paclitaxel are two established anticancer drugs. When used together, they constitute an effective strategy for treating advanced non-small-cell lung cancer (NSCLC). To give full play of these drugs, dual drug-loaded liposome functionalized with non-invasive multimodality imaging contrast agents, can provide both good tumor diagnosis and inhibition and monitoring of the disease treatment. Targeted paclitaxel and carboplatin combinations showed apparent synergic cytotoxicity on non-small-cell lung cancer cells. The T_1 -weighted MRI signal of lung cancer tumor was much stronger after administration of the multifunctional liposome when compared to the contrast agent Omniscan[®] at the same dose. The diagnostic and drug therapy time was also greatly prolonged. Furthermore, the tumor therapy could be monitored non-invasively by MRI in realtime, demonstrating the good performance of the doublet chemotherapy drug delivery liposome on tumor growth inhibition. The characters of nanoparticles and the targeted effect of peptide c(RGDyK) can decrease the dose of the drug and contrast agent greatly, realizing the safe application in animal studies. Drugs combinations can also decrease the dose and the drug resistance. This targeted drug-loaded liposomal system, have good biocompatibility, can successfully

carry both hydrophobic and hydrophilic molecules and be detected by multimodality imaging technologies. Importantly, non-invasive and real-time diagnosis and monitoring of disease development and therapeutic responses by MRI allows for the treatment strategy adjustment, which has great implications for personalized cancer therapy. This delivery system can also be used as an excellent theranostic agent and a promising platform for studying and treating other solid tumors^[41].

Photodynamic therapy (PDT) introduced photosensitizer which inhibits cancer cell growth by generating reactive oxygen species (ROS) after light activating. PDT has been successfully used in a variety of treatments because of its low toxicity to un-irradiated areas. However, laser with high power was always employed because skin and tissues are opaque, and this may also burn the skin. In our study, PDT was combined with photothermal therapy (PTT) and biological redox therapy (BRT) to enhance anti-cancer efficacy, results showed an NIR light with low power could kill cancer cells and inhibit tumor growth^[42]. As shown in Figure 14.12(a), photosensitizer Lu-TP and biological redox drug Gd-TP were loaded onto RGD modified graphene quantum dots (GQD-RGD) via π - π stacking interaction. The nanoconstruct would transport to $\alpha_v\beta_3$ overexpressed cancer cells through the guidance of RGD. After being selectively endocytosed, drugs would be released because of the acidic and hydrophobic surroundings. Gd-TP induced the depletion of intracellular-reducing metabolites and bioenergetics disruption, which broke the protection against oxidative damage from Lu-TP induced ROS. The used NIR laser at 765 nm not only activated the photosensitizer Lu-TP, but also caused the photothermal effect of GQD. The GQD converted the NIR light into thermal energy and heated cancer cell to 43°C. Different from other reported phototherapy, such mild heating would increase membrane permeability and promote probe uptake rather than kill cells directly. The release of drugs also caused “turning on” fluorescence of drugs and GQD at 783nm and 582nm, this lighted the targeted cancer cells. Moreover, the nanoconstruct would shorten the T_1 of water protons and use as a T_1 -weighted MRI contrast agent due to the paramagnetic property of Gd(III). Hence, the nanoconstruct could also act as a probe to monitor cancer cells and the development of tumors. To prove the above designation, we intravenous injected the nanoconstruct to A549 lung tumor bearing mice. *In vivo* fluorescent imaging and MRI results confirmed the enrichment of the nanoconstruct in tumor after 1.5h post injection. Then, the ensured tumor area was treated with the combined therapy,

which induced by the irradiation of a 765nm laser at the power of $300\text{mW}/\text{cm}^2$. The development of tumor was carefully monitored by MRI. Results showed that after three times of treatment, the tumor volume of the BRT/PDT/PTT treated group was decreased to 74% after treatment, in comparison to increased volumes of the BRT group (516%), PDT group (183%) and blank group (819%), respectively, showing a superior synergistic therapeutic effect (Figure 14.12(b)). The dual-modality imaging nanoconstruct enables the synergistic therapy (BRT/PDT/PTT) with dramatically improved efficacy, providing a new approach for cancer treatment and evaluation.

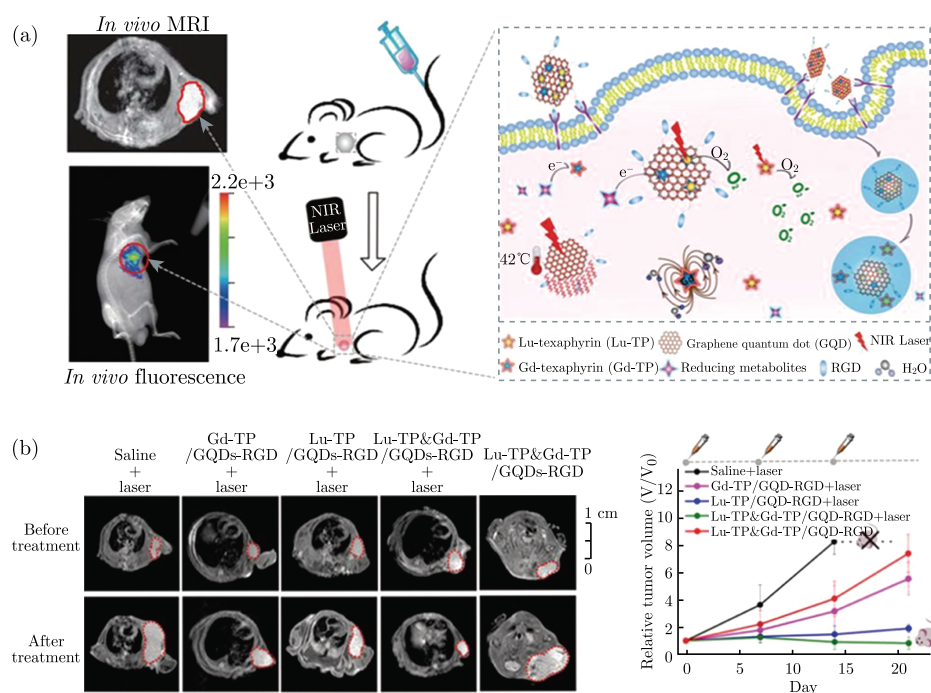


Figure 14.12 (a) Description of nanoconstruct to deliver cancer treatment via biological redox-enhanced photodynamic therapy combined with photothermal heating. (b) The tumor sites were irradiated with a 765nm laser after 1.5h post-injection of the nanoconstruct. Tumor sizes were measured before treatment, and the tumor volumes were normalized to their initial sizes. Antitumor efficiency on A549 implanted mice model was assessed by MRI. Tumors before and after three periods of treatment were marked by the red dotted line. (Figure was adapted with permission from Ref [42], copyright © 2017, American Chemical Society)

14.4 Ultralow field magnetic resonance spectroscopy

Traditional nuclear magnetic resonance spectrometer needs the radio frequency induction coil to detect the nuclear magnetic resonance signal of the sample. Most methods to improve the intensity (to realize high magnetic field and high sensitivity) of MR signal is increasing the magnetic field intensity of the magnet. But the applications and technology promotions of high field NMR spectrometer are limited by the expensive production cost, high maintenance costs, large volume and weight, and difficult maintainability. Research and development of low field NMR will supplement the high field magnetic resonance spectroscopy to some extent. However, the low field NMR also needs to overcome the problem of low polarizability and detection sensitivity. A magnetometer based on superconducting quantum interference device (SQUID) can replace the RF induction coil to realize low magnetic field and high sensitivity NMR detection. However, it still relies on liquid nitrogen or helium to achieve working conditions.

With the birth of the laser and the development of quantum optics, some classical and new phenomena of atomic physics are constantly re-recognized and discovered, such as nonlinear magneto-optical rotation (NMOR), spin exchange relaxation free (SERF). These new physical phenomena have been exploited to produce narrow atomic resonance signals that enable highly accurate measurements of magnetic field^[43-46]. Ultra-low field spectrometers based on atomic magnetometers eliminate the requirement of superconducting magnets with high magnetic fields and do not require ultra-low temperature operating environments to enable highly sensitive NMR detection at zero and/or ultra-low field.

The magnetometers currently used in NMR spectroscopy are primarily based on NMOR and SERF. NMOR magnetometer is mainly used for the determination of ultra-low magnetic field of water and magnetic nanoparticles^[47]. Due to low working temperature (cesium atom, 39°C), NMOR magnetometer has great application prospect in bio-magnetic measurement and magnetic imaging.

SERF magnetometer is mainly used in ultra-low and zero field NMR measurement. Using a SERF magnetometer, the J-coupling spectrum of ethanol was measured at zero magnetic field and the corresponding spectral resolution was 0.1Hz^[48]. Benefit from the spectral resolution, the zero-field J-spectrum enables the distinction of different functional groups^[49] and the residual dipolar coupling of samples^[50].

The combination of SERF magnetometer and NMR achieves zero and ultra-low field NMR studies that enable to study structural and kinetic behavior of chemical and biological molecules in geomagnetic environments. This breakthrough provides a new tool for NMR spectroscopy study^[51].

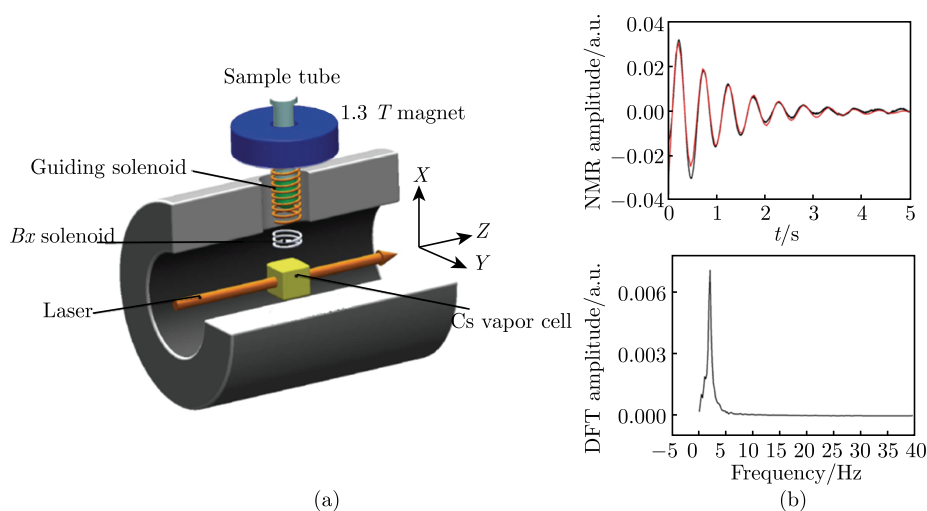


Figure 14.13 (a) A schematic of a laser-probing MR device based on the NMOR laser atomic magnetometer. The sample is first pre-polarized at the pre-polarized magnet outside the magnetic shield to produce a macroscopic, observable magnetization vector. The prepolarized sample is then transported through the injection device to the detection area inside the magnetic shield. In the case of a very small magnetic field, the deflection angle of the linearly polarized light is proportional to the magnetic field strength, so that the NMR signal generated by the sample can be inversely deduced by detecting the deflection angle. (b) ^1H spectrum at ultra-low magnetic field. The leading field of the FID signal is 47nT. The frequency of ^1H spectrum obtained by the resonance signal is 2Hz, and the line width is 0.32Hz. SNR is about 50. (Figure was adapted with permission from Ref [47], copyright ©2013 Elsevier Inc.)

Acknowledgments

We acknowledge the support by the National Natural Science Foundation of China (81227902, 81625011), National Program for Support of Eminent Professionals (National Program for Support of Top-notch Young Professionals) and the Strategic

Priority Research Program of the Chinese Academy of Sciences (XDB21010200). We thank the help from Li Wang, Sa Xiao, Qian Zhou, Maohua Zhu and Tong Li.

References

- [1] R.H. Acosta, P. Blümler, S. Han, S. Appelt, F.W. Häsing, J. Schmiedeskamp, W. Heil, H.W. Spiess, *Magn. Reson. Imaging* 2004. **22**, 1077.
- [2] D. Dupuich, Y. Berthezène, P.L. Clouet, V. Stupar, E. Canet, Y. Crémillieux, *Magn. Reson. Med.* 2003. **50**, 777.
- [3] A.M. Oros, N.J. Shah, *Phys. Med. Biol.* 2004. **49**, 105.
- [4] X. Zhou, Y. Sun, M. Mazzanti, N. Henninger, J. Mansour, M. Fisher, M. Albert, *NMR Biomed.* 2011. **24**, 170.
- [5] T.G. Walker, *Rev. Mod. Phys.* 1997. **69**, 629.
- [6] X. Zhou, D. Graziani, A. Pines, *Proc. Natl. Acad. Sci. USA* 2009. **106**, 16903.
- [7] X. Zhou, X. Sun, J. Luo, X. Zeng, M. Liu, M. Zhan, *Chin. Phys. Lett.* 2004. **21**, 1501.
- [8] X. Zhou, J. Luo, X. Sun, X. Zeng, S. Ding, M. Liu, M. Zhan, *Phys. Rev. B*, 2004. **70**, 052405.
- [9] X. Zhou, Chapter <<Hyperpolarized noble gases as contrast agents>>in book<<In vivo NMR imaging: methods and protocols>>, Humana Press, USA, 2011.
- [10] H. Zhang, J. Xie, S. Xiao, X. Zhao, M. Zhang, L. Shi, K. Wang, G. Wu, X. Sun, C. Ye, X. Zhou, *Med. Phys.* 2009. **45**, 3097.
- [11] H. Deng, J. Zhong, W. Ruan, X. Chen, X. Sun, C. Ye, M. Liu, X. Zhou, *J. Magn. Reson.* 2016. **263**, 92.
- [12] J. Zhong, W. Ruan, Y. Han, X. Sun, C. Ye, X. Zhou, *Sci. Rep.* 2016. **6**, 25854.
- [13] W. Ruan, J. Zhong, Y. Han, X. Sun, C. Ye, X. Zhou, *Chin. J. Magn. Reson. Imaging* 2015. **32**, 262.
- [14] W. Ruan, J. Zhong, K. Wang, G. Wu, Y. Han, X. Sun, C. Ye, X. Zhou, *J. Magn. Reson. Imaging* 2016. **45**, 879.
- [15] W. Ruan, J. Zhong, Y. Guan, Y. Xia, X. Zhao, Y. Han, X. Sun, S. Liu, C. Ye, X. Zhou, *Magn. Reson. Med.* 2016. **78**, 1891.
- [16] H. Li, Z. Zhang, X. Zhao, X. Sun, C. Ye, X. Zhou, *Magn. Reson. Med.* 2015. **76**, 408.
- [17] H. Li, Z. Zhang, X. Zhao, Y. Han, X. Sun, C. Ye, X. Zhou, *NMR in Biomed.* 2018. DOI:10.1002/nbm.3961.
- [18] J. Zhong, H. Zhang, W. Ruan, J. Xie, H. Li, H. Deng, Y. Han, X. Sun, C. Ye, X. Zhou, *NMR Biomed.* 2017. **30**, e3730.
- [19] H. Deng, W. Deng, X. Sun, C. Ye, X. Zhou, *Sci. Rep.* 2016. **6**, 35760.
- [20] H. Deng, W. Deng, X. Sun, M. Liu, C. Ye, X. Zhou, *IEEE Transactions on Biomedical Engineering* 2017. **64**, 1803.

- [21] S. Xiao, H. Deng, C. Duan, J. Xie, H. Zhang, X. Sun, C. Ye, X. Zhou, *J. Magn. Reson.* 2018. **290**, 29.
- [22] M.M. Spence, S.M. Rubin, I.E. Dimitrov, E.J. Ruiz, D.E. Wemmer, A. Pines, S.Q. Yao, F. Tian, P.G. Schultz, *Proc. Natl. Acad. Sci. USA* 2001. **98**, 10654.
- [23] L. Schroder, T.J. Lowery, C. Hilty, D.E. Wemmer, A. Pines, *Science* 2006. **314**, 446.
- [24] J. Zhang, W. Jiang, Q. Luo, X. Zhang, Q. Guo, M. Liu, X. Zhou, *Talanta* 2014. **122**, 101.
- [25] Q. Guo, Q. Zeng, W. Jiang, X. Zhang, Q. Luo, X. Zhang, L.S. Bouchard, M. Liu, X. Zhou, *Chem. Eur. J.* 2016. **22**, 3967.
- [26] S. Yang, Y. Yuan, W. Jiang, L. Ren, H. Deng, L.S. Bouchard, X. Zhou, M. Liu, *Chem. Eur. J.* 2017. **23**, 7648.
- [27] S. Yang, W. Jiang, L. Ren, Y. Yuan, B. Zhang, Q. Luo, Q. Guo, L.S. Bouchard, M. Liu, X. Zhou, *Anal. Chem.* 2016. **88**, 5835.
- [28] Q. Zeng, Q. Guo, Y. Yuan, Y. Yang, B. Zhang, L. Ren, X. Zhang, Q. Luo, M. Liu, L.S. Bouchard, X. Zhou, *Anal. Chem.* 2017. **89**, 2288.
- [29] X. Zhang, K.S. Lovejoy, A. Jasanoff, S.J. Lippard, *Proc. Natl. Acad. Sci. USA* 2007. **104**, 10780.
- [30] G. Yang, L. Wu, B. Jiang, W. Yang, J. Qi, K. Cao, Q. Meng, A.K. Mustafa, W. Mu, S. Zhang, S.H. Snyder, R. Wang, *Science* 2008. **322**, 587.
- [31] S. Zhang, C.N. Ong, H. Shen, *Cancer Lett.* 2004. **208**, 143.
- [32] N. Shao, J. Jin, H. Wang, J. Zheng, R. Yang, W. Chan, Z. Abliz, *J. Am. Chem. Soc.* 2010. **132**, 725.
- [33] M.R. Junttila, F.J. de Sauvage, *Nature* 2013. **501**, 346.
- [34] Y. Wang, K. Zhou, G. Huang, C. Hensley, X. Huang, X. Ma, T. Zhao, B.D. Sumer, R.J. DeBerardinis, J.M. Gao, *Nat. Mat.* 2014. **13**, 204.
- [35] P. Vaupel, F. Kallinowski, P. Okunieff, *Cancer Res.* 1989. **49**, 6449.
- [36] K. Kessenbrock, V. Plaks, Z. Werb, *Cell* 2010. **141**, 52.
- [37] C. Yin, F. Huo, J. Zhang, R. Martinez-Manez, Y. Yang, H.G. Lv, S. Li, *Chem. Soc. Rev.* 2013. **42**, 6032.
- [38] X. Zhu, S. Chen, Q. Luo, C. Ye, M. Liu, X. Zhou, *Chem. Commun.* 2015. **51**, 9085.
- [39] Q. Wang, S. Chen, Q. Luo, M. Liu, X. Zhou, *RSC Adv.* 2015. **5**, 1808.
- [40] L. Ren, S. Chen, H. Li, Z. Zhang, C. Ye, M. Liu, X. Zhou, *Nanoscale* 2015. **7**, 12843.
- [41] L. Ren, S. Chen, H. Li, Z. Zhang, J. Zhong, M. Liu, X. Zhou, *Acta Biomaterialia* 2016. **35**, 260.
- [42] Y. Yang, S. Chen, L. Liu, S. Li, Q. Zeng, X. Zhao, H. Li, Z. Zhang, L.S. Bouchard, M. Liu, X. Zhou, *Acs Applied Materials & Interfaces* 2017. **9**, 23400.
- [43] A.L. Bloom, *Appl. Opt.* 1962. **1**, 61.
- [44] D. Budker, V. Yashchuk, M. Zolotarev, *Phy. Rev. Lett.* 1998. **81**, 5788.

- [45] J.C. Allred, R.N. Lyman, T.W. Kornack, M.V. Romalis, *Phy. Rev. Lett.* 2002. **89**, 130801.
- [46] I.M. Savukov, M.V. Romalis, *Phy. Rev. Lett.* 2005. **94**, 123001.
- [47] G. Liu, X. Li, X. Sun, J. Feng, C. Ye, X. Zhou, *J. Magn. Reson.* 2013. **237**, 158.
- [48] M.P. Ledbetter, *J. Magn. Reson.* 2009. **199**, 25.
- [49] J.W. Blanchard, M.P. Ledbetter, T. Theis, M. C. Butler, D. Budker, A. Pines, *J. Am. Chem. Soc.* 2013. **135**, 3607.
- [50] J.W. Blanchard, T.F. Sjolander, J.P. King, M. Ledbetter, E.H. Levine, V.S. Bajaj, D. Budker, A. Pines, *Phys. Rev. B.* 2015. **92**, 220202.
- [51] M.C.D. Tayler, T. Theis, T.F. Sjolander, J. W. Blanchard, A. Kentner, S. Pustelny, A. Pines, D. Budker, *Revi. Sci. Instruments* 2017. **88**, 091101.

Chapter 15

NMR Applications in Measuring Protein Noncovalent Interactions

Lishan Yao*, Liaoyuan An, Ning Zhang, Jingwen Li, Yefei Wang

Qingdao Institute of Biofuel and Bioprocess Technology, Chinese Academy of Sciences,
266101, P.R.China.

*Correspondence should be sent to: yaols@qibebt.ac.cn

Compared to structural and dynamics of biomolecules, the intra- and inter-molecular interactions are studied far less. These interactions guide protein folding, protein-protein recognition, enzyme-substrate binding, and etc. NMR provides a unique tool to study these interactions at atomic level. In this chapter, we reviewed recent NMR studies of non-covalent interactions in proteins, including h-bond, CH/pi, and electrostatic. The experimental principles are briefly described and their applications are highlighted.

NMR is a powerful tool for studying protein structure and dynamics. The NOE based method, together with residual dipolar coupling, paramagnetic effect, J-coupling and etc., is well developed to determine the protein structure. Meanwhile, the NMR relaxation methods are very effective in characterizing protein dynamics at time scale spanning from picosecond to second. It is known that the property of a protein system is determined by its Hamiltonian, i.e., the interaction between atoms including covalent bond, hydrogen bond (h-bond), electrostatic, van der Waals interaction. Various NMR methods have been developed to measure the noncovalent interactions. In this chapter, NMR applications in this area are reviewed.

15.1 h-bond interaction

H-bonds are important for protein structure and function. Usually, the h-bonds in a protein are identified by spatial proximity, e.g., the distance between h-bond donor and acceptor, from its structure. Direct detection of $^3\text{h}J_{\text{NC}}$ -coupling cross protein backbone h-bond ($\text{N}-\text{H}\cdots\text{O}=\text{C}$) was demonstrated by Grzesiek^[1] and Bax^[2]. The backbone amide ^{15}N magnetization is transferred to the carbonyl ^{13}C of its h-bond partner through a long delay and then the ^{13}C chemical shift is recorded, after which the magnetization is transferred back for ^1H detection. This spectrum contains the chemical shift information about the h-bond donor (H and/or N) and acceptor atoms (C). The size of the $^3\text{h}J_{\text{NC}}$ -coupling can also be determined after recording a reference spectrum where the magnetization is transferred through the one-bond $^1J_{\text{NC}}$ -coupling. To further improve the spectrum sensitivity, a TROSY version of the experiment was also proposed^[3]. A similar method in measuring the $^2\text{h}J_{\text{HC}}$ -coupling was also developed^[4] where the magnetization is transferred from amide ^1H to carbonyl ^{13}C and then back for detection. A strong correlation was observed between $^2\text{h}J_{\text{HC}}$ and $^3\text{h}J_{\text{NC}}$. Due to faster relaxation of the transverse ^1H magnetization, the protein sample has to be deuterated. Even so, the sensitivity of $^2\text{h}J_{\text{HC}}$ is much lower than $^3\text{h}J_{\text{NC}}$. An E.COSY based method was proposed to simultaneously measure $^2\text{h}J_{\text{HC}}$ and $^3\text{h}J_{\text{NC}}$ ^[5]. The advantage of the method is that the sign of $^2\text{h}J_{\text{HC}}$ can be determined by the E.COSY effect. The experiment has a similar sensitivity issue because the $^2\text{h}J_{\text{HC}}$ measurement accuracy strongly depends on the signal-to-noise ratio.

DFT calculations showed that the $^3\text{h}J_{\text{NC}}$ -coupling depends mainly on two parameters, the distance between donor H and acceptor O, and the angle $\angle\text{H}\cdots\text{O}=\text{C}$. An empirical equation was proposed for $^3\text{h}J_{\text{NC}}$ -coupling. The exponential dependence on the O-H distance indicates that $^3\text{h}J_{\text{NC}}$ -coupling decreases very quickly as the distance becomes larger. The angular dependence suggests that the linear configuration with the angle $\angle\text{H}\cdots\text{O}=\text{C}$ equal to 180° yields the largest $^3\text{h}J_{\text{NC}}$ -coupling. This is a bit different from the angular dependence of the h-bond interaction where the angle $\angle\text{H}\cdots\text{O}=\text{C}$ of $\sim 120^\circ$ yields a stronger h-bond strength. This is not surprising since the h-bond strength depends on the overlap between the lone pair electrons of O and the σ^* orbital of H whereas the J -coupling depends on the overlap of the σ orbitals. The linear configuration yields a larger overlap between σ orbitals of the

C=O bond and that of H and thus gives a larger ${}^3\text{h}J_{\text{NC}}$ -coupling. This also explains the strong J -coupling distance dependence.

The precise measurement of ${}^3\text{h}J_{\text{NC}}$ -coupling permits one to capture fine h-bond perturbation by environment e.g., temperature^[6] and pressure^[7]. It is known that protein tends to expand as temperature increases. The determination of ${}^3\text{h}J_{\text{NC}}$ -coupling for each h-bond at different temperatures showed that although ${}^3\text{h}J_{\text{NC}}$ -coupling generally decreases with temperature, the h-bonds are not affected to the same extent by the thermal expansion. This information can help identify protein hotspots, i.e., regions with the least thermostability.

The sensitivity of ${}^3\text{h}J_{\text{NC}}$ experiment can be further enhanced through protein deuteration which slows down the transverse relaxation in the cross-h-bond magnetization transfer. ${}^3\text{h}J_{\text{NC}}$ was measured for unfolded ubiquitin^[8] where values of $\sim 0.05\text{Hz}$ were observed in the N-terminus of ubiquitin, indicating that h-bonds can form even for unfolded proteins.

Besides J -coupling detection for the N—H \cdots O=C h-bond, the observation of C α —H α \cdots O=C J -coupling (${}^3\text{h}J_{\text{C}\alpha\text{C}'}$) was also reported although the values are generally smaller^[9]. A negative correlation was observed between the N—H \cdots O=C and C α —H α \cdots O=C J -couplings, indicating that N—H and C α —H α compete for the same h-bond acceptor. Due to faster relaxation of C α and CO, the sensitivity of $J_{\text{C}\alpha\text{C}'}$ is lower than that of ${}^3\text{h}J_{\text{NC}}$.

H-bond between the lysine side chain NH_3 and the backbone C=O was also observed by the ${}^3\text{h}J_{\text{N}\zeta\text{C}'}$ -coupling^[10]. Unlike the backbone N—H \cdots O=C h-bond which is generally rigid, the $\text{NH}_3\cdots\text{O}=\text{C}$ is more mobile and thus the amplitude of ${}^3\text{h}J_{\text{N}\zeta\text{C}'}$ is smaller. Due to fast exchange of amino protons with water, the TROSY based experiment can not be applied for the ${}^3\text{h}J_{\text{N}\zeta\text{C}'}$ detection. Instead, proton decoupling was applied in the buildup of $\text{N}\zeta\text{C}'$ magnetization to keep the $\text{N}\zeta$ magnetization in-phase. To slowdown the proton exchange, the measurement needs to be performed at low pH and temperature.

Computational studies indicate that backbone h-bonds are cooperative in α -helix^[11-14]. But the direct experimental proof of H-bond cooperativity is difficult to obtain. A NMR H/D exchange method was proposed to measure the α -helix (A23-D36) h-bond cooperativity of protein GB3^[15], with the principle described as follows. Due to the Ubbelohde effect^[16], the substitution of ${}^1\text{H}$ by ${}^2\text{H}$ in a backbone N—H \cdots O=C H-bond weakens the H-bond strength^[17-19] by shortening the N—H

bond length and thus lengthening the H—O distance^[17,20]. The shortening of N—H bond length is caused by the anharmonic vibration of the N—H bond where the heavy ²H decreases the vibration amplitude which effectively moves ²H closer to N than ¹H. The distance change alters the electron distribution of N—H···O=C while the surrounding nuclei respond by adjusting their electron density and thus geometry (including h-bonds) to minimize the total potential energy. The change of electron density around the surrounding nuclei also changes their chemical shifts (H/D isotope effect). By measuring the chemical shift changes of surrounding nuclei, the information of H-bond cooperativity can be extracted.

Figure 15.1 shows the [¹H, ¹⁵N] chemical shift changes of Y33 at two temperatures, 275 K (a, b) and 298 K (c, d). At 275K, the peak position shifts with the H/D exchange, although the intensity of the peak is unchanged, indicating that the

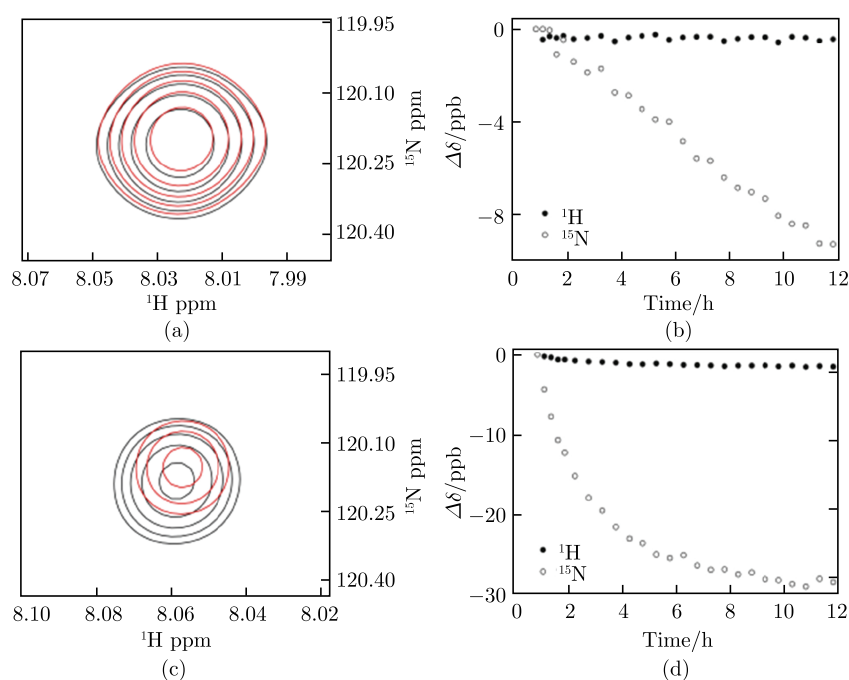


Figure 15.1 ¹H, ¹⁵N chemical shift perturbation $\Delta\delta$ of residue Y33 in WT GB3. (a), (c) Overlay of the Y33 ¹H—¹⁵N HSQC signals of the first (grey) and the last (red) spectrum of a recorded time series: (a) 275 K; (c) 298 K. The corresponding $\Delta\delta$ time profiles are shown in (b) 275 K, and (d) 298 K. (Figure was adapted with permission from Ref [21], copyright © 2016, American Chemical Society)

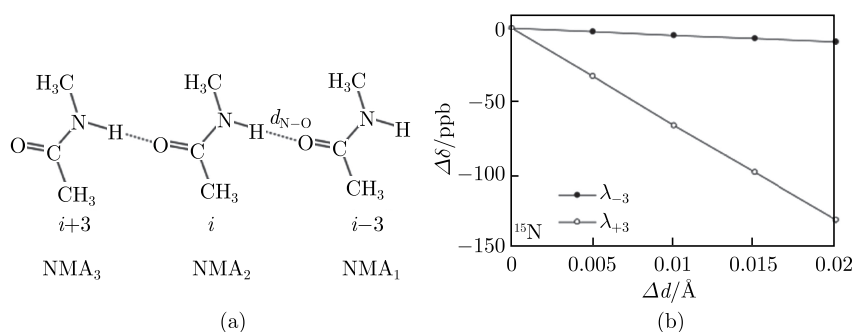
H/D exchange rate of Y33 is very slow. The peak position shift is attributed to the H/D exchange of D36. At 298K, both the position and the intensity of the peak change with time, suggesting that the H/D exchange occurs for the amide of Y33. At the same time, the isotope effect is also observed.

This chemical shift change $\Delta\delta$ can be fitted using the following equation:

$$\Delta\delta_i(t) = \delta_i(t) - \delta_i(t_0) = c \sum_{j=1}^n \lambda_{ij} [\exp(-k_j t) - \exp(-k_j t_0)] \quad (1)$$

where $\delta_i(t)$ is the ^{15}N chemical shift at time t , λ_{ij} is the ^{15}N chemical shift change of site i due to the H/D exchange of amide site j , t_0 and t represent the midpoints of the first and subsequent HSQC measurements, k_j is the H/D exchange rate of site j measured separately from the decaying intensity of the signal of amide j , and c is the fraction of the D_2O in the $\text{H}_2\text{O}/\text{D}_2\text{O}$ solvent. In principle, the coupling information between any two amides can be extracted using this equation. However, the degeneracy arises if different sites have similar exchange rates. To solve this problem, the exchange rate was measured at different temperature and pH conditions and also mutations were introduced to perturbation the exchange rates of nearby amides. Moreover, an assumption was made that λ_{ij} is solely dependent on the separation, l , of helical residues i and j , i.e. on $l = j - i$. The fitting suggests that λ values can be retrieved for $l = -3$ to $+3$. The absolute values of λ from the sites with $l > 0$ (negative) are much larger than those with $l < 0$.

DFT calculations were performed to help understand λ values. The QM calculations show that increasing the h-bond length between i and $i - 3$ yields negative λ values, with λ_{+3} more negative than λ_{-3} , consistent with the experimental observation (Figure 15.2). Furthermore, the QM calculations indicate that the negative λ



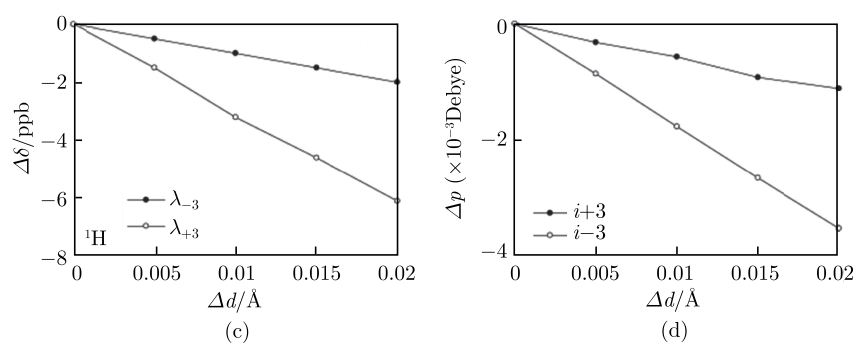


Figure 15.2 Quantum mechanical calculations of the H-bonding effect on chemical shifts and dipole moments in a model tri-NMA complex. (a) The peptide plane H-bond geometry. The calculated λ values of (b) ^{15}N and (c) ^1H of NMA1 (λ_{+3}) and NMA3 (λ_{-3}) decrease as the distance increases. (d) The accompanying decrease in dipole moments of NMA1 and NMA3 indicates a weakening of the polarization of these two peptide planes. Figure was adapted with permission from Ref [21], copyright © 2016, American Chemical Society.

values correspond to a decrease of the peptide plane electric dipole moment (Figure 15.2(d)), which thereby weakens its H-bonding and electrostatic interactions with other peptide planes. In summary, the H-bonding cooperativity in the α -helix of protein GB3 can readily be studied by the H/D exchange NMR method.

15.2 C-H/ π interaction

The CH/ π interaction, referring to the interaction between a CH group and a π system (e.g., an aromatic side chain), is very common in proteins. It is essentially the interaction between π electrons and the σ^* orbital of H. The double mutational cycle (DMC) method can be used to measure the strength of CH/ π interactions. But the method implicitly assumes that the protein structure is unchanged by mutation and any secondary effect can be cancelled out. Practically, the mutation of an aromatic residue can significantly destabilize the protein which may not be able to fold properly. The DMC measurement error can compromise the accuracy of CH/ π , especially the weak ones.

Direct detection of CH/ π has been reported recently^[22] between aliphatic methyl groups and aromatic side chains. The magnetization starts from methyl and then transfers to the carbon of aromatic group where its chemical shift is recorded. Then, the magnetization transfers back to the methyl for direct ^1H detection. The methyl

group is particularly suited for this type of measurement because its relaxation rate can be greatly reduced through the methyl TROSY type of experiment^[23] where the C—H/C—H and H—H/H—H dipole-dipole relaxations cancel out. Furthermore, the methyl group has three hydrogens so that its magnetization is three times as large as e.g., the backbone amide N—H.

$^{\text{h}\pi}J_{\text{CMeCaro}}$ values up to 0.3Hz were detected between methyl carbon and aromatic carbon atoms for model proteins ubiquitin and GB3. Meanwhile, $^{\text{h}\pi}J_{\text{HMeCaro}}$, i.e., J-coupling between methyl hydrogen and aromatic carbon atoms was also detected. Using $^{12}\text{CH}_3$ labeled methyl groups, the relaxation during the $\text{H}_{\text{Me}}\text{C}_{\text{aro}}$ magnetization transfer can be further slowed down (^{13}C chemical shift anisotropy relaxation contribution no longer exists) which permits measurement of J-coupling as small as 0.03Hz.

More recently, the CH/ π interaction between methyl and carbonyl was also studied by measuring the J-coupling between methyl hydrogen and carbonyl carbon^[24]. According to DFT calculations, $^{\text{n}\pi}J_{\text{HmeCO}}$ is much smaller (in mHz range) thus detecting this type of CH/ π is more challenging. Nevertheless, the observation of $^{\text{n}\pi}J_{\text{HmeCO}}$ suggests that CH/ π interactions also exist between C-H and carbonyl groups.

15.3 Electrostatic interaction

Electrostatic interactions are important to maintain protein structure and facilitate its function. Electrostatic interactions between ionizable residues can be measured by the NMR pKa titration experiment. To probe the electrostatics, the ionization state of a residue is usually changed by mutagenesis and then the pKa changes of nearby ionizable residues are measured. These pKa changes correspond to the charge-charge interaction between the mutated residue and the detected ionizable residues^[25].

In pH titration NMR experiments, the chemical shifts of ionizable residues (e.g., the side chain carboxyl group ^{13}C) are recorded. These chemical shifts can be fitted by the following equation,

$$\delta_{\text{obs}} = \frac{\delta_{\text{AH}} + \delta_{\text{A}}10^{n(\text{pH}-\text{pKa})}}{1 + 10^{n(\text{pH}-\text{pKa})}} \quad (2)$$

where δ_{AH} and δ_{A} are the chemical shifts of the ionizable residue when it is protonated and deprotonated, respectively. n is the Hill constant, accounting for the

nonideality of the fitting curve. The fitting of the chemical shift yields the pKa of the ionizable pKa.

Coulombic interactions in the protein staphylococcal nuclease (SNase) have been studied systematically. Δ pKa values of histidine residues have been determined at different salt conditions^[25]. It is shown that a simple coulombic potential, with a Debye-Huckel term, is capable to describe the experimental data very well, suggesting that the protein surface charge-charge interaction is very water-like. On the other hand, the electrostatic calculations based on the finite-difference solution of the Poisson-Boltzmann (FDBP) equation have to use a large dielectric constant (~ 20) for the protein to reproduce the experimental data. The use of the unrealistically large dielectric constant for the protein (instead of the normal value of $2\sim 4$) implies that the dielectric constant of the protein water interface is underestimated and the protein relaxation caused by the ionization state change is not accounted properly by FDBP.

The NMR pKa method can also be used to study the short-range charge-charge coupling^[26]. In the active site of *Bacillus circulans* xylanase, the catalytic acid E172 and the nucleophile E78 are $\sim 5.5\text{\AA}$ apart and strongly coupled. The side chain carboxyl chemical shift titration curve has to be fitted to more sophisticated equations which help disentangle the coupling between two charges. The pKa change of the two catalytic residues along the reaction path illustrates the enzyme catalytic process.

One limitation of the NMR pKa titration method is the measurement accuracy. Acid or base was added to the NMR sample to adjust the pH which can be monitored by a pH meter. A small pH drift ($\sim 0.1\sim 0.2$ pH units) can always be seen when the sample is transferred in and out of the NMR tube after titration. This drift is difficult to eliminate practically. Furthermore, the pH meter usually can measure the pH to the accuracy of 0.1 pH units (or ~ 0.02 pH units in favorable cases). As a result, the pKa reported for charged residues of the same protein can vary by ~ 0.1 pH or larger^[27]. To eliminate the pH measurement error contribution to Δ pKa, our group developed a new NMR titration method, as described by follows, to study the salt bridge interactions in protein GB3^[28]. Taking the salt bridge H31-E27 as an example, the H31-E27 sample was $^{15}\text{N}/^{13}\text{C}$ labeled whereas the H31-Q27 mutant was ^{15}N labeled only. The two samples were mixed together and titrated by HCl or NaOH. The backbone [^1H , ^{15}N] chemical shifts of H31-E27 and H31-Q27 were

recorded by an interleaved pulse sequence which separates the signals of two proteins using an isotope filter. Because the two proteins were dissolved in the same tube, the pH measurement error does not affect ΔpKa . As a result, the accuracy of ΔpKa can be greatly improved.

The ΔpKa values were measured for four salt bridges, H4-E15, H28-E24, H31-E27, and H50-D47 at different temperatures. These ΔpKa values were then fitted to the Van't Hoff equation, $-2.303\Delta\text{pKa} = \Delta H/RT - \Delta S/R$ to yield enthalpy (ΔH) and entropy (ΔS) values. It turns out that all four salt bridges have positive ΔH and ΔS , suggesting that the salt bridge formation is driven by entropy^[28]. It is a bit counterintuitive because one would expect that the Coulomb attraction should yield a negative ΔH and the restraining of the protein side chains should yield a negative ΔS .

Molecular dynamics simulations provide more insights into the formation mechanism. The calculated change of enthalpy and entropy agrees with the experimental result. The advantage of MD simulation is that the enthalpy and entropy changes ΔH and ΔS can be further decomposed to two components, the contribution from the protein, ΔH_{prot} and ΔS_{prot} , and that from the solvent water, ΔH_{solv} and ΔS_{solv} . The negative ΔH_{prot} indicates that the protein enthalpy decreases (due to Coulomb attraction between two opposite charges) as the salt bridge is formed. But the positive ΔH_{solv} suggests that the formation of the salt bridge decreases the two charges' interaction with solvent water. The net effect is that the enthalpic loss by the solvent surpasses the enthalpic gain by the protein, so that the total enthalpy change is unfavorable for the salt bridge formation. From the entropic point of view, the negative ΔS_{prot} is consistent with the argument that the protein degrees of freedom are restrained after the salt bridge formation. In contrast, the positive ΔS_{solv} implies that the solvent entropy increases. As the charges' interaction with the solvent water becomes weaker the water molecules are less restrained so that the entropy of these water molecules increases. The total entropy change ΔS is positive, indicating that the entropic gain by the solvent is larger than the entropic loss by the protein. The total entropic gain is also greater than the enthalpic loss. Thus, it is the entropy that drives the formation of salt bridges. Although the salt bridges formed by histidine are far less than those by lysine or arginine, the mechanism of the salt bridge formation should be very similar. All four salt bridges characterized in GB3 are on protein surface. As for more buried salt bridges, the water contribution to the total

enthalpy and entropy change should decrease. One would expect that the enthalpic gain from the protein may play a more favorable role. For salt bridges deeply buried in proteins which are usually destabilizing, the change of enthalpy and entropy can be very different from that of the surface salt bridges. More works will be needed to understand the thermodynamics of buried salt bridges.

15.4 Electric field

It is known that electric field (e-field) affects the nuclear chemical shift. According to Buckingham, this effect can be expressed by a power series in the field^[29-30]. The e-field in proteins is very non-uniform, therefore it is nearly impossible to obtain the e-field on a nuclear from a single chemical shift. In practice, a designed e-field is introduced by mutating a neutral residue to a charged one (e.g., A to K) or through pH titration^[31]. At the same time, the chemical shift changes are recorded by the ¹H–¹⁵N HSQC spectrum for the backbone amides. These chemical shift changes are caused by the introduction of the charge. This experiment greatly simplifies the complex e-field created by all the charges and polar residues in the protein^[32]. Through this method, apparent dielectric constants of 3 to 13 were obtained for charges of different proteins^[32]. One caveat of the method is that the introduction of a charge also perturbs the protein structure. As a result, the chemical changes also have contributions from structural perturbation which complicates the data analysis process. The value of the apparent dielectric constant can be contaminated by the structural perturbation effect.

A protocol was developed by us to measure the long-range amide ¹H_N chemical shift changes caused by e-field^[33]. Using protein GB3 as a model, a single charged residue mutation K19A was made. For nuclei far away from K19, the structure perturbation is smaller and the chemical shift perturbation (CSP, $\Delta\delta$) is mainly from the e-field effect. Since the CSPs are also smaller for remote nuclei, it is necessary to measure the CSPs with very high accuracy. To do so, the mutant K19A (¹⁵N labeled) and the wild type (WT, ¹⁵N/¹³C labeled) GB3 were mixed and dissolved in the same NMR buffer. The chemical shifts were recorded using an interleaved ¹H–¹⁵N HSQC experiment^[33]. Since the WT but not the mutant K19A is ¹³C labeled, a ¹³C isotope filter was introduced to select the signal from WT or K19A. To minimize the structural perturbation effect on CSP, only amides more than 12Å away from

K19 were collected for the e-field analysis whereas the CSPs from the nuclei closer to K19 were thrown away. Meanwhile, another mutation K19E was also introduced. The CSPs of K19E and those of K19A were correlated, with a slope of 1.8, close to the net charge change ratio (2:1), indicating that the long-range CSPs are due to the e-field of K19.

$\Delta\delta$ was then fitted by using the Buckingham equation. By systematically adjusting ε_a , the difference between experimental and predicted $\Delta\delta$ can be minimized which yield an apparent dielectric constant of 8.8. It is known that a protein powder sample has a dielectric constant of 2~4, thus it is obvious that the water molecules contribute to the apparent dielectric constant. MD simulation was performed for the WT, K19A, and K19E mutants. By explicitly calculating the long-range electric field created by the introduced charge K19 or E19, and by the corresponding reorganization of water molecules, it can be seen that the screening by the water reorganization is quite large, ~ 4 ^[33]. Apparently, water molecules can play an important role in the e-field screening. It is expected that for sites with different water accessibilities, the apparent dielectric constant can vary dramatically.

According to the Kirkwood–Fröhlich formalism^[34–36], dielectric constant of a molecule depends on the fluctuation of molecular dipole and the temperature. MD simulations show that protein dielectric constant increases with the temperature^[37]. This increase is mainly caused by the enhanced fluctuation of charged side chains at high temperature. The temperature effect on protein apparent dielectric constant was also studied by measuring CSPs from 278K to 313K. As temperature increases, CSPs generally become smaller, suggesting that the apparent dielectric constant increases with temperature^[33]. It is known that water dielectric constant decreases with temperature, opposite to that of a protein. It becomes difficult to determine how big the two effects are in reality. Another likely effect is that the side chain conformation is extended at high temperature so that the water contribution is larger and the electrostatic screening is stronger. Although the exact temperature dependent mechanism for the apparent dielectric constant is still unknown, it has to be explicitly considered when studying temperature dependent protein electrostatic properties.

The electrostatic interaction is greatly affected by ionic strength. To estimate the salt effect on e-field, CSPs were measured at different ion concentrations. At higher salt concentration, the CSPs are smaller, corresponding to a weaker e-field. The

Debye-Huckel theory helps evaluate the ion effect on electrostatics, but the equation was derived for low concentration free ions. For charges on protein surface, the ionic effect is more complicated because the inner part of a protein is not accessible to ions. Nevertheless, the ionic strength dependence of the CSPs strongly suggests that the e-field is also greatly affected by ions in solution^[33].

The advantage of CSP measurement is that it is highly accurate. For protein GB3, amide ¹H CSPs can be measured to the accuracy of ~ 0.3 ppb, which permits one to capture the fine CSP perturbation due to environmental changes. This method was used to probe the cell lysate effect on the protein e-field. The interior of a cell is very crowded, with macromolecules such as protein, DNA, and RNA that can reach concentration up to 400g/L^[38]. One prominent question is whether the crowded cell environment affects protein structure, interaction and function. It was proposed that the biomolecules in cell tend to form so called quinary interactions with the targeted protein and thus affect its function. The transient quinary interaction is difficult to capture and its effect on protein is largely unknown although it has been suggested that protein electrostatics can be affected by quinary interactions^[39].

We used GB3 as a model system and studied molecular crowders' effect on protein e-field^[40]. We selected three sites 10, 19, and 40 and measured e-field from both the positive charge (K) and the negative charge (D or E). The molecular crowders included dextran, Ficoll, protein BSA, and *E.coli* lysate. The residues show that Ficoll and dextran have no effect on CSPs, suggesting the e-field is not affected by these two crowders. Ficoll and dextran are the so called "inert crowder" which tends to decrease the entropy of proteins through the volume exclusion effect. As such, they have no effect on enthalpy of proteins and thus electrostatics. In comparison, the CSPs are scaled down by BSA. For example, in 90 g/L BSA, the CSPs are reduced by $\sim 4\% \sim 6\%$ for $\Delta\delta_{A10K}$, $\Delta\delta_{D40A}$, and $\Delta\delta_{D40K}$, and $\sim 7\% \sim 8\%$ for $\Delta\delta_{A19K}$ and $\Delta\delta_{E19K}$ whereas for $\Delta\delta_{E10K}$ the CSPs are reduced by $\sim 26\%$ ^[40]. These data suggest that different sites and charges respond differently to BSA. CSPs are further reduced in the presence of lysate, with the largest effect from $\Delta\delta_{A19K}$ by 67%. Both BSA and lysate are capable to reduce the e-field, suggesting that the transient quinary interaction, which is absent in dextran and Ficoll, causes the protein electrostatic property change.

Chemical shifts are sensitive to local environmental change. If BSA or lysate binds to GB3, one would expect to see chemical shift changes especially for the

binding region. However, no significant chemical shift changes were observed for particular residues, suggesting that the interaction with GB3 is very weak. In contrast, if mapping the binding chemical shift difference between the WT and the mutant (e.g. K10A), outliers close to the mutational site are observable. It becomes clear that the mutation affects the transient interaction with GB3. The change of the quinary interaction caused by mutation can also be probed by backbone ^{15}N relaxation rates. Quinary interaction with lysate tends to dramatically increase the transverse relaxation rate R_2 because the protein sizes in lysate are generally much larger than GB3 whereas the effect on the longitudinal rate R_1 is smaller. Thus, the product R_1R_2 can be used as an indicator for the quinary interaction^[41]. The difference ΔR_1R_2 ($\Delta R_1R_2 = R_1R_2(\text{mut}) - R_1R_2(\text{WT})$) between the WT and a mutant indicates whether the mutated residue directly interacts with crowders. The ΔR_1R_2 shows that the largest change comes from K19A/E, consistent with the CSPs data.

It is important to understand the quinary interaction mechanism. The weakening of the e-field suggests that this interaction has the electrostatic origin. Meanwhile, ions such as NaCl also weaken e-field and this weakening is originated from electrostatics according to Debye-Huckel theory. The chemical shift changes caused by lysate are compared with those by NaCl. A strong correlation was observed for residue K10, and a moderate correlation was observed for K19 and D40, suggesting that the e-field weakening mechanism by lysate is similar to that by NaCl. That is to say, the electrostatic potential created by a charged side chain (e.g. K19) causes the redistribution of lysate on GB3 surface which in turn creates a reaction field screening the field by the charge. But this is a very qualitative explanation for the e-field weakening by quinary interactions. More quantitative models will be needed to understand how a protein structure and its charge distribution are affected by lysate or its constituent proteins.

In this chapter, we have reviewed the NMR studies of noncovalent interactions in proteins. NMR is a particularly powerful tool for this kind of studies because measurables such as chemical shift and J-coupling contain rich information about the site-specific interactions in proteins. Many developed methods are tested only on well-behaved model proteins with good relaxation properties. More studies are needed for functional proteins and enzymes, as well as other biomolecules such as DNA and RNA.

References

- [1] F. Cordier, S. Grzesiek, Direct observation of hydrogen bonds in proteins by interresidue $(3h)J(NC')$ scalar couplings. *J. Am. Chem. Soc.*, 1999. **121**(7), 1601-1602.
- [2] G. Cornilescu, J.S. Hu, A. Bax, Identification of the hydrogen bonding network in a protein by scalar couplings. *J. Am. Chem. Soc.*, 1999. **121**(12), 2949-2950.
- [3] Y.X. Wang, J. Jacob, F. Cordier, P. Wingfield, S.J. Stahl, S. Lee-Huang, D. Torchia, S. Grzesiek, A. Bax, Measurement of $(3h)J(NC')$ connectivities across hydrogen bonds in a 30 kDa protein. *J. Biomol. NMR*, 1999. **14**(2), 181-184.
- [4] F. Cordier, M. Rogowski, S. Grzesiek, A. Bax, Observation of through-hydrogen-bond $(2h)J(HC')$ in a perdeuterated protein. *Journal of Magnetic Resonance*, 1999. **140**(2), 510-512.
- [5] A. Meissner, O.W. Sorensen, New techniques for the measurement of $C'N$ and $C'H-N$ J coupling constants across hydrogen bonds in proteins. *Journal of Magnetic Resonance*, 2000. **143**(2), 387-390.
- [6] F. Cordier, S. Grzesiek, Temperature-dependence properties as studied by of protein hydrogen bond high-resolution NMR. *J. Mol. Biol.*, 2002. **317**(5), 739-752.
- [7] L. Nisius, S. Grzesiek, Key stabilizing elements of protein structure identified through pressure and temperature perturbation of its hydrogen bond network. *Nature Chemistry*, 2012. **4**(9), 711-717.
- [8] S. Meier, M. Strohmeier, M. Blackledge, S. Grzesiek, Direct observation of dipolar couplings and hydrogen bonds across a beta-hairpin in 8 M urea. *J. Am. Chem. Soc.*, 2007. **129**(4), 754-755.
- [9] F. Cordier, M. Barfield, S. Grzesiek, Direct observation of C-alpha-H-alpha center dot center dot O=C hydrogen bonds in proteins by interresidue $(h3)J(C\ \alpha\ C')$ scalar couplings. *J. Am. Chem. Soc.*, 2003. **125**(51), 15750-15751.
- [10] L. Zandarashvili, D.W. Li, T.Z. Wang, R. Bruschweiler, J. Iwahara, Signature of Mobile Hydrogen Bonding of Lysine Side Chains from Long-Range N-15-C-13 Scalar J-Couplings and Computation. *J. Am. Chem. Soc.*, 2011. **133**(24), 9192-9195.
- [11] R. Wieczorek, J.J. Dannenberg, H-bonding cooperativity and energetics of alpha-helix formation of five 17-amino acid peptides. *J. Am. Chem. Soc.*, 2003. **125**(27), 8124-8129.
- [12] R. Wieczorek, J.J. Dannenberg, Hydrogen-bond cooperativity, vibrational coupling, and dependence of helix stability on changes in amino acid sequence in small 3(10)-helical peptides. A density functional theory study. *J. Am. Chem. Soc.*, 2003. **125**(46), 14065-14071.
- [13] N. Kobko, L. Paraskevas, E. del Rio, J.J. Dannenberg, Cooperativity in amide hydrogen bonding chains: Implications for protein-folding models. *J. Am. Chem. Soc.*, 2001. **123**(18), 4348-4349.
- [14] A.V. Morozov, K. Tsemekhman, D. Baker, Electron density redistribution accounts for

- half the cooperativity of alpha helix formation. *J. Phys. Chem. B*, 2006. **110**(10), 4503-4505.
- [15] T.S. Ulmer, B.E. Ramirez, F. Delaglio, A. Bax, Evaluation of backbone proton positions and dynamics in a small protein by liquid crystal NMR spectroscopy. *J. Am. Chem. Soc.*, 2003. **125**(30), 9179-9191.
- [16] A.R. Ubbelohde, K.J. Gallagher, Acid-Base Effects in Hydrogen Bonds in Crystals. *Acta Crystallogr*, 1955. **8**(2), 71-83.
- [17] V.A. Jaravine, F. Cordier, S. Grzesiek, Quantification of H/D isotope effects on protein hydrogen-bonds by (h3)J(NC ') and (1)J(NC ') couplings and peptide group N-15 and C-13 ' chemical shifts. *J. Biomol. NMR*, 2004. **29**(3), 309-318.
- [18] S. Grzesiek, F. Cordier, V. Jaravine, M. Barfield, Insights into biomolecular hydrogen bonds from hydrogen bond scalar couplings. *Progress in Nuclear Magnetic Resonance Spectroscopy*, 2004. **45**(3-4), 275-300.
- [19] B.A. Krantz, A.K. Srivastava, S. Nauli, D. Baker, R.T. Sauer, T.R. Sosnick, Understanding protein hydrogen bond formation with kinetic H/D amide isotope effects. *Nat. Struct. Biol.*, 2002. **9**(6), 458-463.
- [20] G. Cornilescu, B.E. Ramirez, M.K. Frank, G.M. Clore, A.M. Gronenborn, A. Bax, Correlation between (3h)J(NC ') and hydrogen bond length in proteins. *J. Am. Chem. Soc.*, 1999. **121**(26), 6275-6279.
- [21] J.W. Li, Y.F. Wang, J.F. Chen, Z.J. Liu, A. Bax, L.S. Yao, Observation of alpha-Helical Hydrogen Bond Cooperativity in an Intact Protein. *J. Am. Chem. Soc.*, 2016. **138**, 1824-1827.
- [22] M.J. Plevin, D.L. Bryce, J. Boisbouvier, Direct detection of CH/pi interactions in proteins. *Nature Chemistry*, 2010. **2**(6), 466-471.
- [23] J.E. Ollerenshaw, V. Tugarinov, L.E. Kay, Methyl TROSY: explanation and experimental verification. *Magn. Reson. Chem*, 2003. **41**(10), 843-852.
- [24] F.A. Perras, D. Marion, J. Boisbouvier, D.L. Bryce, M.J. Plevin, Observation of CH center dot center dot center dot pi Interactions between Methyl and Carbonyl Groups in Proteins. *Angewandte Chemie-International Edition*, 2017. **56**(26), 7564-7567.
- [25] K.K. Lee, C.A. Fitch, B. Garcia-Moreno, Distance dependence and salt sensitivity of pairwise, coulombic interactions in a protein. *Protein Sci.*, 2002. **11**(5), 1004-1016.
- [26] L.P. McIntosh, D. Naito, S.J. Baturin, M. Okon, M.D. Joshi, J.E. Nielsen, Dissecting electrostatic interactions in *Bacillus circulans* xylanase through NMR-monitored pH titrations. *J. Biomol. NMR*, 2011. **51**(1-2), 5-19.
- [27] J.H. Tomlinson, S. Ullah, P.E. Hansen, M.P. Williamson, Characterization of Salt Bridges to Lysines in the Protein G B1 Domain. *J. Am. Chem. Soc.*, 2009. **131**(13), 4674-4684.
- [28] N. Zhang, Y.F. Wang, L.Y. An, X.F. Song, Q.S. Huang, Z.J. Liu, L.S. Yao, Entropy Drives the Formation of Salt Bridges in the Protein GB3. *Angewandte Chemie-*

- International Edition, 2017. **56**(26), 7601-7604.
- [29] A.D. Buckingham, Chemical Shifts in the Nuclear Magnetic Resonance Spectra of Molecules Containing Polar Groups. *Can. J. Chem.*, 1960. **38**(2), 300-307.
- [30] A.D. Buckingham, K.P. Lawley, Nuclear Magnetic Shielding of a Hydrogen Atom in (1) an Electric Field-Gradient and (2) a Cage. *Mol Phys*, 1960. **3**(3), 219-222.
- [31] M.A.S. Hass, M.R. Jensen, J.J. Led, Probing electric fields in proteins in solution by NMR spectroscopy. *Proteins-Structure Function and Bioinformatics*, 2008. **72**(1), 333-343.
- [32] P. Kukic, D. Farrell, L.P. McIntosh, E.B. Garcia-Moreno, K.S. Jensen, Z. Toleikis, K. Teilum, J.E. Nielsen, Protein Dielectric Constants Determined from NMR Chemical Shift Perturbations. *J. Am. Chem. Soc.*, 2013. **135**(45), 16968-16976.
- [33] L.Y. An, Y.F. Wang, N. Zhang, S.H. Yan, A. Bax, L.S. Yao, Protein Apparent Dielectric Constant and Its Temperature Dependence from Remote Chemical Shift Effects. *J. Am. Chem. Soc.*, 2014. **136**(37), 12816-12819.
- [34] H. Fröhlich, *Theory of Dielectrics*. Oxford University Press, London, U.K.: 1958.
- [35] M. Neumann, Dipole-Moment Fluctuation Formulas in Computer-Simulations of Polar Systems. *Mol. Phys.*, 1983. **50**(4), 841-858.
- [36] J.G. Kirkwood, The dielectric polarization of polar liquids. *J. Chem. Phys.*, 1939. **7**(10), 911-919.
- [37] J.W. Pitera, M. Faltus, W.F. van Gunsteren, Dielectric properties of proteins from simulation: The effects of solvent, ligands, pH, and temperature. *Biophys. J.*, 2001. **80**(6), 2546-2555.
- [38] S.B. Zimmerman, S.O. Trach, Estimation of Macromolecule Concentrations and Excluded Volume Effects for the Cytoplasm of Escherichia-Coli. *J. Mol. Biol.*, 1991. **222**(3), 599-620.
- [39] W.B. Monteith, R.D. Cohen, A.E. Smith, E. Guzman-Cisneros, G.J. Pielak, Quinary structure modulates protein stability in cells. *Proc. Natl. Acad. Sci. U. S. A.*, 2015. **112**(6), 1739-1742.
- [40] N. Zhang, L. An, J. Li, Z. Liu, L. Yao, Quinary Interactions Weaken the Electric Field Generated by Protein Side-Chain Charges in the Cell-like Environment. *J. Am. Chem. Soc.*, 2017. **139**(2), 647-654.
- [41] Y.Q. Wang, C.G. Li, G.J. Pielak, Effects of Proteins on Protein Diffusion. *J. Am. Chem. Soc.*, 2010. **132**(27), 9392-9397.

Chapter 16

Application of Nanodiscs in Examining Protein-Membrane Interaction

Yujuan Wang¹, Junfeng Wang^{1,2,*}

¹ High Magnetic Field Laboratory, Key Laboratory of High Magnetic Field and Ion Beam
Physical Biology,

Hefei Institutes of Physical Science, Chinese Academy of Sciences, 230031;

² Institute of Physical Science and Information Technology, Anhui University, 230601,
Hefei, Anhui, P. R. China.

*Correspondence should be sent to: junfeng@hmfl.ac.cn

Membrane proteins play very important roles in metabolism, signaling, cell motility, transport, development, and many other biochemical and biophysical processes on molecular level throughout the life circle. Detailed understanding of these processes is necessary for the progress of life sciences and biomedical applications. The newly developed nanodiscs provide a new and powerful tool for biochemical and biophysical studies of membrane proteins because they are commonly acknowledged as an optimal membrane mimetic system that provides controlled size, composition, and specific functional modifications on the nanometer scale. In this chapter, we'll attempt to introduce the structure and assembly of nanodiscs, the use of nanodiscs for structural studies of membrane proteins briefly. And we'll mainly focus on the introduction of advantages provided by nanodiscs as a new tool to examine protein-membrane interactions at High magnetic field laboratory of Chinese academy of sciences.

16.1 Introduction to nanodiscs

Membrane proteins are represented by a tremendous variety of sizes, structures,

and functions, including complex supramolecular hierarchical assemblies with dozens of proteins forming sophisticated molecular machines. Most of important cellular functions, including oxidative phosphorylation and proton pumping, ATP synthesis, transport of metabolites, intra- and inter-cellular signaling, membrane fusion and communication between cell compartments, the biosynthesis of many compounds including lipids, steroid hormones, and the breakdown of xenobiotics and internal metabolites need the participation of membrane proteins. Membrane proteins also conduct developmental processes, including cell motility, adhesion, recognition, neuronal patterning, and many other critical events. The first line of sensing and defense for the cell response to injury, environmental stress, and viral infections are provided by membrane proteins. Membrane proteins are also directly involved in many other processes essential for cell function. Four Nobel prizes awarded for the discovery of membrane protein in the last 15 years emphasize that the biophysics, biochemistry, structural biology, and cell biology of membrane proteins represent a very broad and significant part of modern life science research.

Investigations centering on membrane biophysics and biochemistry include structural studies using a variety of techniques. Lots of researches are focusing on revealing overall dynamics and functionally important motions, in order to define the affinity and selectivity of ligand binding, both as substrates and allosteric modulators, goals of understanding the chemistry of enzymatic catalysis, the nature of energy transduction, and the generation of motility and the movement of ions and molecules by transporters and channels. Often these critical cellular functions are conducted by supra-molecular complexes of protein, lipid, and nucleic acid. Some of these properties can be studied using purified proteins in the absence of membrane. However, many of the aspects critical for membrane protein structure and function depend on the lipid environment. Most membrane proteins are misfolded or display altered activity if removed from their native membrane environment. Sometimes specific lipids are needed for membrane-centered processes such as the blood coagulation cascade enabled by exposure to an anionic surface. The regulatory role of cardiolipin in the function of some transporters, roles for phosphoinositides in the recruitment of activating proteins that control the formation of focal adhesions in cell migration, and the formation of complex signaling structures mediated by electrostatic factors are a few examples.

Substantial progress has been made in recent years in developing lipid bilayer

or mimetic membrane for appropriate analysis of membrane proteins^[1-5]. The most frequently used model membranes nowadays are liposomes, detergent-stabilized micelles and disc-shaped bicelles. Membrane proteins in detergent micelles are prone to altered conformational dynamics, misfolding, and dysfunction^[6]. Liposomes, vesicles composed of synthetic lipid bilayers, are good mimetics of the native lamellar membrane. And they can provide an inside vs. outside compartmentalization and a large bilayer area that can allow mobility of multiple proteins and lipids. However, there are many disadvantages when using vesicle systems. The large size of proteoliposomes (Membrane protein-containing liposomes) makes them unsuitable for many spectroscopic techniques due to light scatter and low rotational mobility. These model membranes often display various particle size distributions and have a tendency to segregate into phase separated domains, both in terms of composition and structural heterogeneity. Bicelles and similar extended bilayer structures have been successfully used in some nuclear magnetic resonance (NMR) applications to circumvent those disadvantages. Except bicelles are inherently unstable, the use of detergent might destabilize membrane proteins and even induce error conformation of membrane protein *in vitro*.

The choice of a suitable membrane mimicking environment is of fundamental importance for the characterization of structure and function of membrane proteins. Phospholipid bilayer nanodisc, a monodisperse, stable model membrane, provides a “native-like” lipid bilayer environment (Figure 16.1)^[7,8]. Nanodiscs are now a commonly accepted method for a large variety of biophysical and biochemical studies of membrane proteins. Several groups, including Sligar’s and Wagner’s, are working on engineering of the ApoA1 protein to provide homogeneous particles of defined size and composition. The progresses are useful for empty nanodiscs assembling and

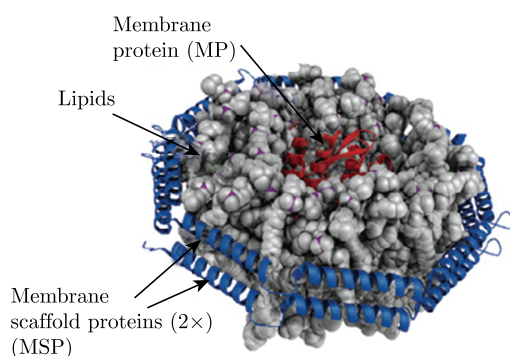




Figure 16.1 Schematic representation of the nanodisc system (top) and the different MSP constructs that have so far been used for NMR-based studies (bottom). Figure was adapted with permission from Ref [9], copyright © 2016, Biological Chemistry.

self-assembling membrane proteins into the bilayer and thus enabling subsequent biochemical and biophysical efforts.

16.2 Self-assembly of nanodiscs

Sligar and co-workers originally developed the nanodisc technology^[10,11] to support the study of the hepatic microsomal NADPH-cytochrome P450 reductase. Nanodiscs are usually composed of phospholipids surrounded by amphipathic apolipoproteins, normally called membrane scaffold proteins (MSPs). The phospholipids and MSPs are arranged in a discoidal bilayer^[12]. The initial MSPs based on the sequence of the human serum apolipoprotein A-I (ApoA1)^[13] provide a hydrophobic surface facing the lipids, and a hydrophilic surface at the outside. This composition makes nanodiscs highly soluble in aqueous solutions and enables the solubilization of embedded membrane proteins without detergents^[10,14]. The size of the nanodisc particles normally span between 6 and 17nm in diameter, depending on the used variant of MSP^[15,16].

Empty nanodiscs can be assembled from a detergent solubilized mixture of all components by gradual removal of detergent via adsorption on hydrophobic beads or by dialysis. In brief, the solution of purified MSP was mixed with cholate-solubilized lipids at optimal molar ratios (1:50~1:80). After incubating at optimal temperature (often at phase transition temperature), bio-beads were added or dialysis initiate the self-assembling process. Gel filtration is often used to separate nanodiscs with other fraction. The use of MSP variants with different length and the choice of different molecular ratio between MSP and phospholipids will impact the nanodiscs diameter. If this ratio is lower or higher than optimal, the size and composition dis-

tributions of the resulting nanodiscs are broader, and their stability is compromised. Otherwise, in order to mimic membrane fraction from different organelle, several kinds of phospholipid can be mixed together to obtain nanodiscs by incubate the mixture at proper temperature. At this moment, the differences of phase transition temperature should be considered carefully.

This self-assembly protocol of nanodiscs with membrane in it is relatively complicated^[9]. The specific details may vary according to the properties of membrane proteins, the yield and properties of the final product can be optimized by changing the important parameters. The details include temperature, time, molecular ratio of MSP to membrane protein and phospholipids, detergent used for incorporating membrane protein. The choice of detergent for incorporating a membrane protein target into nanodiscs depends on the properties of the membrane protein. The best ratios for a specific membrane protein-nanodiscs system should be empirically optimized around the expected values. For this, size exclusion chromatography (SEC) can be used as a readout to optimize towards homogenous particles of the expected size. The properties of detergent for incorporating a membrane protein also should be mutually soluble with detergent used to solve phospholipids. The methods and procedure for removing detergent also should be considered. For membrane proteins preferred monomeric or oligomeric state, the molecular ratio of MSP, lipids and target membrane protein, as well as the mode of incorporation into the bilayer needs to be optimized. As far as oligomeric channels are concerned, the occupation of membrane proteins to replace the amounts of phospholipid should be addressed. In other words, the lipid/MSP stoichiometry is also critical, which means the number of lipids displaced by the membrane protein from the nanodiscs bilayer must be estimated and subtracted from the initial number of lipids in the corresponding empty nanodiscs. For incorporating TRPV1 into nanodisc, the MSP to TRPV1 ratio was kept at 1.5:1 to 1:1^[17]. But for reconstitution of β 2-adrenergic receptors utilizing self-assembling Nanodisc technology, the ratio of MSP1: β 2AR was 150:1^[18].

Finally, some specific chaperones, cofactors including some kinds of special phospholipid should also be considered adding to the mixture to improve the efficiency of self-assembly. At last, the isolation and purification method used to obtain the final product is also very important. Chromatography, density ultracentrifugation, or other methods can be used according to certain membrane proteins. Sometimes,

several methods should be combined together to improve the yield of nanodiscs incorporated membrane proteins.

16.3 Properties of nanodiscs

Since nanodiscs were introduced to the research of membrane protein, lots of efforts were made to optimize MSP protein and protocols for forming highly homogeneous, stable, and monodisperse nanodiscs with controlled size. Sliger's and Wagner's groups undertook an extensive effort to generate variants based on the original human ApoA1 sequence. As an example, Sliger's lab designed a series of extended scaffold proteins with one, two, or three additional 22-mer amphipathic helices inserted in the central part of MSP1 (designated MSP1E1, MSP1E2, and MSP1E3 correspondingly)^[8] and studied the self-assembly of discoidal particles. Wagner's lab developed smaller nanodiscs mainly for NMR application displaying faster tumbling rates and improved spectral resolution with deletions of the amphipathic helices in the center of MSP, e.g. MSP1D1 Δ H5 and MSP1D1 Δ H4-6^[19] as shown in figure 16.1. Some other labs reported deletions of C-terminal helices^[16,20]. All the nanodiscs were shown to form discs of 6~10nm in diameter.

Nanodiscs of various sizes can be assembled using MSP with appropriate length. Longer MSPs can be used to assemble nanodiscs up to ~17nm diameter^[15]. Compared with standard nanodiscs, covalently circularized nanodiscs can be obtained by sortase, exhibit enhanced stability, defined diameter and tunable shapes^[21]. Numerous biophysical methods including size exclusion chromatography, free-flow electrophoresis, mass spectrometry, and electron microscopy can be used to quantitate the monodisperse nanodiscs^[22-25]. And some other structural methods used to characterize nanodiscs include transmission electron microscopy (TEM), cryoelectron microscopy (cryo-EM), small angle solution X-ray (SAXS) and neutron (SANS) scattering.

Lots of reports about the structure of nanodiscs and of membrane proteins inserted in the bilayer were investigated by NMR. Both solid state NMR (ss-NMR) and solution NMR methods were used to study empty nanodiscs. Some details of lipid MSP interactions and some of the physiologically important interactions of lipid head-groups with cations in solution were revealed by ss-NMR^[26-28]. The configuration of the protein backbone obtained by ss-NMR was consistent with the "belt" model of MSP, rather than the "picket fence" configuration proposed in the earlier

literature for rHDL particles^[27].

The rotational correlation time is indeed important for NMR study of proteins. Smaller nanodiscs are prior to the big ones for high-resolution NMR spectroscopy by increasing rotational mobility. The rotational correlation times for nanodiscs consisting MSP1D1 in aqueous solution at 45°C were estimated to be ~55-60 ns^[29]. This makes it suitable for acquisition of NMR spectra of membrane proteins in nanodiscs using TROSY pulse sequences and NMR spectrometers operating a field of 800MHz or higher. Wagner and co-workers first reported the use of nanodiscs assembled by truncated MSPs (MSP Δ H5) and the incorporating membrane protein in it^[19].

For nanodiscs with special lipid compositions and also with incorporated membrane proteins, the application of free flow electrophoresis can be chosen for preparative or analytical separation, especially for the three scaffold proteins, MSP1D1, MSP1D1 without the His-tag, and MSP1E3D1, having slightly different pKa, and hence charge, at neutral pH^[22]. The separation of nanodiscs with P450 reductase from empty nanodisc assembled with neutral POPC was very efficiency by using this method. The method offers a new choice complementary to size-exclusion chromatography.

Mass spectrometry (MS) has emerged as a powerful tool to study membrane protein complexes and protein-lipid interactions. Native mass spectrometry and nanodisc mass spectrometry were also developed to study intact nanodiscs. Lipid composition can be determined by using a dual Fourier transform approach to obtain the average lipid mass. Further, the effects of lipid head group chemistry on nanodisc dissociation mechanisms can be determined by investigating the relationship between gas-phase behavior, lipid composition, and instrumental polarity.

16.4 Application of nanodiscs for studies of membrane proteins

Nanodiscs have been widely used in the researches on membrane protein, includes the application for structural studies, lipid and protein interactions and molecular screening.

16.4.1 Structural study of membrane proteins

Ever since the nanodiscs technique was developed, researchers started to try using

it to obtain critical structural data of membrane protein. The first choice is the use of nanodiscs for determining the crystal structure of membrane proteins. But the results were less than satisfactory. Many investigators use assembly into nanodiscs to store and collect active materials for subsequent investigation and functional studies, because the target of interest in nanodiscs is active, monodisperse, and stable to storage and concentration. However, direct crystallization of proteins in the nanodisc has been challenging for the azimuthally disorder of membrane protein in nanodiscs and the mobility of membrane protein above gel-liquid phase transition^[30-32].

With the technical breakthrough in both source and detector, dramatic advances in cryo-electron microscopy have allowed atomic resolution images to be obtained. This also helps the use of nanodiscs in structural studies. More and more beautiful high-resolution structures of membrane protein structures are reported using EM, for example, the structure of the TRPV1 ion channel in the unliganded, agonist-bound, and antagonist-bound states at resolutions of 3.2, 2.9, and 3.4Å^[33], the structure of the Tc toxin at an average resolution 3.46Å in POPC nanodiscs^[34], the 4.2Å-resolution structure of the transmembrane domains of nucleotide-free MsbA^[35].

NMR is a powerful tool for determining membrane protein structures at atomic resolution. Nanodiscs offer additional options to study membrane protein functions and structures besides the widely used micelle and bicelle systems. Both solid state NMR and solution NMR have been used to research on membrane protein. For example, the complete three-dimensional structure of OmpX in nanodiscs by solution NMR demonstrated the value in revealing subtle conformational divergences when in the native bilayer environment^[36]. A direct comparison of the membrane protein BamA and thenerotrophin receptor p75NTRc from rat135 in different membrane mimetics illustrated the enablement of this approach for structural determination^[37]. The research on GPCR antibody was also improved by nanodiscs for the providing of native-like membrane. After selectively isotopically labeling monomeric leukotriene B4 receptor (BLT2), the NMR spectra of BLT2 obtained in nanodiscs with various CHS content showed a redistribution of the BLT2 receptor between four conformational substrates observed in the absence of the ligand^[38].

16.4.2 Molecular spectroscopy of membrane protein

Spectroscopic methods are very useful because they are a mainstay for determining critical functional aspects of many membrane proteins. Due to their lack of

turbidity and low viscosity, nanodiscs provide especially significant advantages for spectroscopic investigations. This makes the fast mixing methods applicable which can be used to monitor structural and functional properties of the incorporated membrane protein by optical methods.

Resonance Raman, optical, and electron spin resonance spectroscopies (ERR) spectroscopy can be used to trap the membrane protein intermediates in nanodiscs at cryogenic temperatures and the stability nanodiscs at cryogenic temperatures. The orientation of cytochrome P450 CYP3A4 in nanodisc POPC membrane measured by using linear dichroism spectroscopy of nanodiscs absorbed on an optical glass waveguide was good agreement with the simulation results^[39]. Besides the widely used EPR and DEER (double electron-electron resonant)^[40-44], fluorescence quenching of Trp235 residue interacting with the membrane by pyrene incorporated in the lipid bilayer was used to measure the extent of membrane insertion^[45]. CD spectroscopy, site-specific fluorescent labeling and fluorescence correlation spectroscopy (FCS) were all reported useful for membrane protein in nanodiscs^[46-55].

X-ray and neutron scattering have been successfully used to characterize membrane proteins in nanodiscs. The so called “silent nanodiscs” where lipid and MSP are contrast matched so only the target protein is observable in a SANS experiment are really useful. SAXS of membrane proteins incorporated in nanodiscs were reported for cytochrome CYP3A4, bR, and the rhodopsin monomer^[7,56-58].

16.4.3 Application of nanodiscs in examining protein-membrane interaction

16.4.3.1 Nanodiscs preparation for NMR research

The assembly of the nanodiscs system requires a number of steps that should be carefully considered to obtain optimal system. Several important steps will be roughly discussed below.

Choosing the MSP

The choice of the MSP should be carefully and specifically evaluated according to each application. Structural researches by solution NMR prefer smaller nanodiscs assembled by shorter MSP in order to reduce the rotational correlation time and thus increase spectral resolution and sensitivity^[19,59]. If the target is large integral membrane protein, MSP1D1E3 is often preferred^[60]. Besides the smaller MSP mentioned

above, Wagner's group just published their researches on covalently circularized nanodiscs. The covalently circularized nanodiscs by sortase exhibit enhanced stability, defined diameter sizes and tunable shapes. Membrane proteins reconstitution in it show enhanced NMR spectra quality for both VDAC-1, a β -barrel membrane protein, and the G-protein-coupled receptor ntr1. And the advantages of covalently circularized nanodiscs also help to visualize how simple, nonenveloped viruses translocate their genomes across membranes to initiate infection^[21]. Another choice is amphipathic 22-residue peptide (PVLDFRELLNELLEALKQKLK), which can also assemble lipid-bilayer-containing nanodiscs. The reconstitution of the P450-cytb5 complex in peptide-based nanodiscs has been demonstrated, which are characterized by size exclusion chromatography and NMR spectroscopy^[61].

Choosing the lipids

The choice of lipids in nanodiscs is of particular importance to obtain/maintain the target membrane protein in its native conformation. In general, lipid composition of biological membranes is similar between different cell types or membrane types of one cell, but may also change over time, e.g. during the life cycle of the cell. Nanodiscs can provide precisely lipid composition mimic membrane lipid that are stable overtime. The mimic membrane's properties can be modulated according to different purpose, including bilayer thickness, charge and fluidity.

Besides the standard phospholipids DMPC, DPPC or POPC, some other special phospholipids have also been successfully incorporated into nanodiscs, including with phospholipid alkyl chains ranging from dilauroyl (DL, 12 carbons) to dielaidoyl (DE, 22 carbons), including unsaturated chains like dioleoyl^[20], and polar head groups varying from phosphocholine (PC, zwitterionic) to phospho-L-serine (PS, negatively charged) in different proportions up to 100% negative charges^[62-67]. Moreover, some minority phospholipids were reported to be assembled in nanodiscs, including cardiolipin up to 10%^[64,68,69], ganglioside GM1 up to 15%^[70,71], sphingomyelin up to 30%^[72] or cholesterol up to 30%^[10,73]. Radio-labeled lipids, lipids with fluorescence, ¹H NMR and HPLC-MS, analytical ultracentrifugation or ion exchange chromatography are suggested to check the lipid content and homogeneity^[11,74,75,76]. In order to improve the membrane protein activity as well as sample quality, stability and NMR behavior, the role of unsaturation, cholesterol or head groups' negative charges should be considered^[59,77,78]. Sometimes, using native membranes extract is more

powerful for the membrane protein, which can be done by extracting lipids from the native cell membrane and using them as precursor for assembly with detergent purified membrane protein^[79,80], or by directly solubilizing protein-containing membrane fractions with detergent and replacing the detergent with suitable MSP^[81].

Choosing the MSP-to-lipid and MSP-to-MP (membrane protein) ratios

For empty nanodiscs, getting monodispersed samples in high yield requires usage of a suitable ratio between the MSP and the lipids during the assembly process. The absolute concentrations of MSP and lipids during assembly are critical, and a minimum lipid concentration of 4mM is recommended^[11,18]. It is better to calculate the ratio from the length of MSP used and chosen lipid first. When membrane proteins are incorporated in nanodiscs, the bilayer area that will be occupied by the protein should be reduced^[60,82]. For example, one needs to remove around 37 DMPC molecules to compensate for bacteriorhodopsin insertion^[7].

In addition to the MSP/lipid ratio, the ratio of MSP to target protein (MSP/MP) can be critical to obtain nanodisc samples of good quality. The number of membrane proteins in nanodiscs is (partly) depended by the ratio of MSP to target membrane^[65,77,83].

Removing detergent

With the development of nanodiscs, more and more researchers realize that an appropriate detergent removal protocol (including speed, ways and temperature) plays a key role in the nanodiscs's auto-assembly reaction. Detergent removal initiates the nanodisc assembly process. Besides the frequently used sodium cholate^[14], sodium dodecylsulfate (SDS) or other detergents can be used as well^[84]. The two most common ways of detergent removal are dialysis and adsorption by bio-beads. The rate of detergent removal determines the overall yield and the sample homogeneity of the resulting nanodiscs^[8]. Prolonged dialysis with two or three changes of buffer, or overnight use of adsorbent beads without agitation are common procedures besides gentle agitation for a few hours. For some systems, it is recommended to use a two steps protocol of 10%~20% w/v bio-beads (first step over-night without shaking, second step 2~3h with shaking after bio-beads exchange).

Temperature

Another important factor affecting nanodiscs assembling efficiency is the tem-

perature, because it will be related to the rate of detergent removal and the lipid bilayer phase. Usually it is recommended to carry out the reaction just below the phase transition temperature of the lipids which favors formation of the nanoscale bilayers.

16.4.3.2 Dynamics of membrane proteins in nanodiscs

Beyond the 3D structure studies mentioned above, NMR-based study can also help fully understanding the functional mechanisms of membrane proteins in a native environment by offering knowledge of the dynamic processes underlying conformational changes or ligand recognition. For example, the authors found the different time scales of dynamic behavior for the BamA β -barrel and its extracellular 'lid loop' L6 by solution NMR investigation of the insertase BamA in micelles, bicelles and nanodiscs^[37,85]. These atomic level founding helped to explain the functional mechanism and the reason of poor electron densities in BamA crystal structures.

16.4.3.3 Interaction studies

Nanodiscs are generally accepted as an ideal tool to study the functional and structural properties of membrane proteins in lipid environment, under defined conditions^[76]. As reviewed by Schuler^[86], nanodiscs also offer good properties to examine protein-protein interactions and lipid-protein interactions. Several important factors influence the interactions will be briefly addressed, including the impact of phospholipids, ions in buffer, diameter of nanodiscs and the small molecular like chaperon.

If the lipid selection is mentioned, liposome pull down (or liposome binding) is also a convenient method to evaluate the lipid specificity of membrane protein. In brief, ultra-centrifuge and SDS-PAGE is used to detect the binding of membrane protein and liposome with specific lipid by collecting the supernatant(S) and precipitant(P). For example, the result that the SNX16PX_CC R121E mutant showed significantly reduced binding capacity to the negatively charged liposome containing 3% PI3P, 67% POPC, and 30% POPS illustrated the non-specific electrostatic interactions might be important for initiating membrane binding of SNX16. The significantly reduced binding capacity of SNX16PX_CC F220E mutant to negatively charged liposomes proved that, the hydrophobic residues F220 and F2200 would penetrate into the hydrophobic region of the lipid bilayer and enhance the interaction

with membrane^[87]. Another example about the binding specificity of *Escherichia coli* UbiG and human and yeast Coq3 to PG (phosphatidylglycerol) or CL (cardiolipin, or diphosphatidylglycerol) also provide new clues for the structural related function explanation^[88].

Both integral membrane protein and membrane-associated protein need proper phospholipid to keep the structure and function. In other words, phospholipid is of great importance for the membrane's related function during life cycle. Some early investigations on cytochrome P450s with membrane reconstitution systems suggested that trace amounts of phospholipids were required for optimal activity^[89], while others suggested that the presence of specific phospholipids might stabilize some kinetically distinguishable conformations of P450s, such as the major drug-metabolizing isoform CYP3A4, and directly modulate its affinity for particular substrates^[90,91]. The type of phospholipid chosen for membrane protein study is important, including both phospholipid head and the chain length. The head group identity (variable size and charge distribution), and acyl chain properties (variable lengths and degrees of saturation) affect the features of biomembrane. Membrane proteins from different organelle need specific types of phospholipid to accomplish the function. Sometimes, lipid mixture is necessary for the special function of membrane proteins. The thickness of membrane offered by nanodiscs should also be considered by using phospholipid with different chain length. Modulations of bacteriorhodopsin (PR) by different lipid composition have also been assessed in Nanodiscs constructed with DMPC or POPC. And the difference in hydrophobic mismatch between the bilayer thickness and the length of the PR transmembrane helices also plays an important role in the observed variations of the photophysical properties^[92].

Besides interacting with the inserted proteins, the metal ions in buffer also affect lipid-protein interactions for lipid head groups may also interact with ions and influence the function of protein. Calcium is the second messenger of signal out of cell and physiological and biochemical reaction in cell. For instance, the ³¹P chemical shift anisotropy is used to probe the change in response to Ca²⁺ addition^[17].

Besides phospholipid and ions, the diameter of nanodiscs also has impact on the protein-lipid interaction. For some protein with high molecular weight, the nanodiscs diameter should be considered for the tumbling rates may affect the spectrum quality of protein.

16.4.3.4 Nanodiscs studies in High magnetic field laboratory in the Chinese academy of sciences

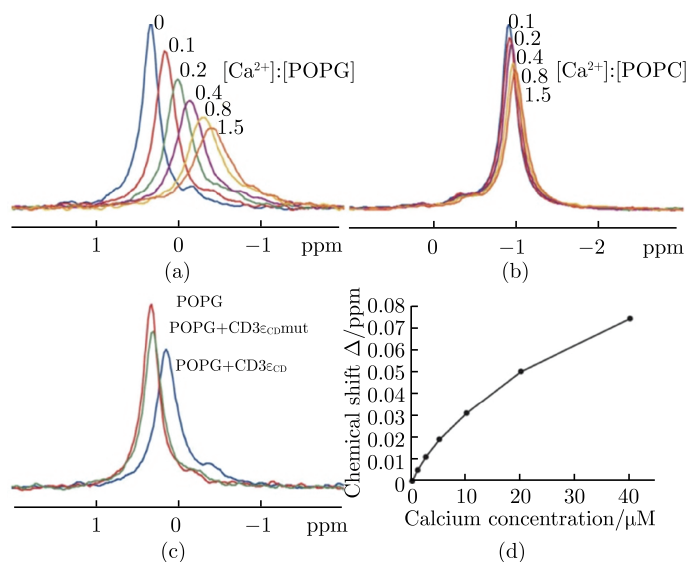
As far as researchers in High magnetic field laboratory in the Chinese academy of sciences realized that nanodiscs will be powerful tool for membrane protein study, the use of nanodiscs has started. The first step was the establishment and the optimization assembling of nanodiscs. Following the experimental procedures from Sligar's lab, the empty nanodiscs were obtained successfully with MSP1D1. The properties of nanodiscs acquired studied by dynamic light scattering (DLS) and TEM were consistent with those reported previously. The diameter of nanodiscs determined by using both negative-staining TEM and DLS is about 20nm.

As mentioned above, smaller nanodiscs are more suitable for the structural and functional studies of membrane protein by using NMR. Enormous efforts have been made to minimize the size of the protein-nanodisc complexes in order to decrease the rotational correlation time and obtain high resolution spectra, because the line widths of NMR resonances will get broader as the size of the protein studied increases. Just like the other labs attempts on nanodiscs, a work to modify α -helical amphipathic protein to obtain smaller size nanodiscs with various lipid compositions started since 2011. The smaller nanodiscs are assembled by Δ MSP, a MSP1D1 mutant where the helix 0.5 and helix 7 to helix 10 segments were deleted. From the nanodiscs assembling and TEM results, the deletion of the last four helices doesn't change the disc-like morphology of nanodiscs. The Δ MSP mutant provides smaller nanodiscs and improved spectrum quality as demonstrated here and by other groups^[11-13], which will broaden the NMR applications of nanodiscs in membrane protein studies. The nanodiscs with varied particle sizes can be obtained by using MSP with different length and by fine-tuning the ratio of scaffold protein to lipids. Nanodiscs with larger diameter could be helpful for other biochemical or biophysical studies, as exemplified in the application of solid state NMR. The further use of the smaller nanodiscs is the successfully incorporating the trans-membrane domain of Stromal Interaction Molecule 1 (STIM1) in it. The use illustrates a good potential of applying smaller nanodiscs in studying trans-membrane protein structures by solution NMR^[16].

As we know, many biochemical processes occur on the surface of a membrane. Communication between the inside and outside of a cell or organelle requires in-

teraction with the membrane surface. The biochemistry processes need membrane proteins (including membrane-associated proteins) and proper membrane composition to accomplish the function. Ionic protein–lipid interactions are crucial for the recognition of structure and function of membrane receptors, ion channels, integrins and many other membrane proteins and membrane associated proteins^[93-96]. The study on how CD3_{CD} dissociates from the membrane in antigen-stimulated T cells provides a new regulatory mechanism of Ca²⁺ to T-cell activation involving direct lipid manipulation using nanodiscs (Figure 16.2). The second messenger Ca²⁺ plays an important part during the process. Ca²⁺ regulates T cell receptor activation by modulating phospholipids electrostatic property. Compared to zwitterionic phospholipids (like PC), spectroscopy showed that Ca²⁺ bound to the phosphate group in anionic at physiological concentrations. The bounding thus further neutralizes the negative charge of phospholipids. It means that calcium can disrupt ionic CD3_{CD}-membrane interaction. Rather than initiating CD3 phosphorylation, this regulatory pathway of Ca²⁺ has a positive feedback effect on amplifying and sustaining CD3 phosphorylation and should enhance T-cell sensitivity to foreign antigens^[97].

For some membrane associated protein, the use of nanodiscs in studying interaction between membrane and protein offers great advantage as they provide a means for precisely controlling the composition of a membrane area. The use of nanodiscs makes it possible to accomplish the interaction researches by microscale



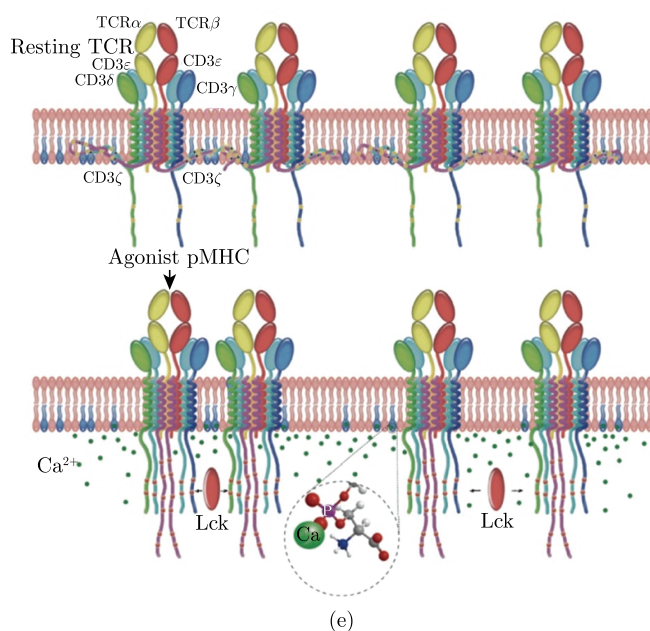


Figure 16.2 Ca^{2+} bound to the phosphate group of anionic phospholipids at physiological concentrations. (a)~(d), One-dimensional ^{31}P NMR experiments were performed to probe the local chemical environment change of the phospholipid phosphate group induced by the binding of Ca^{2+} or $\text{CD3}\epsilon_{\text{CD}}$ peptide. A lipid nanodisc system was used to provide a membrane bilayer environment without the interference of detergent molecules. (e), A schematic illustration of the Ca^{2+} induced TCR signaling amplification model. In the resting state, the positively charged $\text{CD3}\epsilon/\zeta$ cytoplasmic domains interact with anionic phospholipids in the inner leaflet of the plasma membrane and key tyrosine residues are sequestered in the membrane bilayer, which provides a ‘safety’ control on TCR triggering. (Figure was adapted with permission from Ref [97], copyright © 2012, Nature)

thermophoresis (MST), surface plasmon resonance^[18] and isothermal titration calorimetry^[60]. Herein, nanodiscs are used as a controlled membrane surface, to investigate the interaction of granuphilin-C2A domain with PI (4,5)P2 in the phospholipid bilayer environment. The interactions of granuphilin with PIP2 lipids in nanodiscs were studied by NMR methods including chemical shift perturbation and paramagnetic relaxation enhancement. And the study provided key information for evaluating the structural model of PIP2 binding site in the membrane binding C2A domain (Figure 16.3)^[98]. At first, the interactions between protein and PIP2 were characterized by size exclusion chromatography using nanodiscs as the

membrane mimetic system. Then, NMR titration experiments were performed to gain further insights into the interaction details of granuphilin-C2A domain with PI(4,5)P2-nanodisc at the residue-specific level. And the difference in intensity reduction ratio for individual residue at 0.2 equivalent molar ratio of PI(4,5)P2-nanodisc to granuphilin-C2A was analyzed. The results turned out that, besides residues within the concave groove that are responsible for PI(4,5)P2 head group binding, the strand $\beta 5$ was involved in the interaction with the phospholipid bilayer or undergo a small conformation change upon membrane binding. This region may be involved in direct binding to membrane and/or undergo conformation changes upon membrane binding.

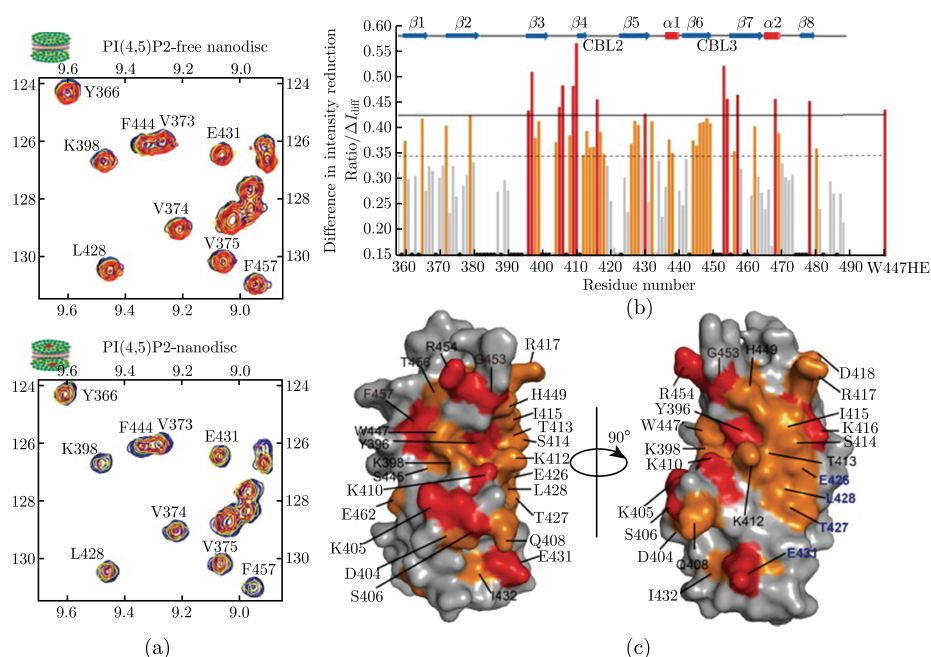


Figure 16.3 NMR investigation of the interaction between granuphilin-C2A domain and PI(4,5)P2-nanodisc. (a) Portion of ^1H - ^{15}N HSQC spectra of granuphilin-C2A in the presence of PI(4,5)P2-free nanodisc (upper panel) and PI(4,5)P2-nanodisc (lower panel). The molar ratios of nanodisc to protein are as following: 0:1 (black), 0.1:1 (blue), 0.2:1 (yellow) and 0.3:1 (red). The cartoon representations of PI(4,5)P2-free nanodisc and PI(4,5)P2-nanodisc are inserted. (b) Differences in the intensity reduction ratio values (ΔI_{diff}) plotted for each residue. (c) Residues with large ΔI_{diff} are mapped on the surface of granuphilin-C2A, using the same color representations as in (b). Residues from the strand $\beta 5$ are labeled in blue. (Figure was adapted with permission from Ref [98], copyright © 2015, Chemistry and Physics of Lipids)

Conclusion

As outlined above, nanodiscs provide optimal stable membrane mimetic system with controlled size, composition, and specific functional modifications on the nanometer scale. Because of these advantages of providing a near native local environment, nanodiscs were widely used in biochemical and biophysical studies of membrane proteins, including the structural, dynamics studies of membrane proteins and interactions between lipid and protein.

The combination of solution NMR and nanodiscs offers new option for the research of peptide or protein-membrane interactions. Solution NMR is the unique way to provide atomic resolution information of protein-membrane or protein-protein interaction in solution. And nanodiscs offer an ideal platform assembled with desired different lipids. If sample preparation is successful and the NMR spectra is decent, membrane proteins assembled in nanodiscs can be used to study interactions between membrane protein-membrane protein, lipid-membrane proteins. Besides interaction studies, nanodiscs can be used to measure residual dipolar couplings (RDCs) using established alignment media and dynamic nuclear polarization (DNP) experiments.

In a word, due to the intrinsic superiorities of nanodiscs and the recent progress in membrane proteins studies, it can be anticipated that nanodiscs will become more and more popular in the NMR-based studies of membrane proteins in a near native environment.

References

- [1] N. Planchard, et al., The Use of Amphipols for Solution NMR Studies of Membrane Proteins: Advantages and Constraints as Compared to Other Solubilizing Media. *Journal of Membrane Biology*, 2014. **247**(9-10): p. 827-842.
- [2] L.A. Baker, and M. Baldus, Characterization of membrane protein function by solid-state NMR spectroscopy. *Curr Opin Struct Biol*, 2014. **27**: p. 48-55.
- [3] L. Maler, Solution NMR studies of peptide-lipid interactions in model membranes. *Mol Membr Biol*, 2012. **29**(5): p. 155-176.
- [4] J.L. Popot, Amphipols, nanodiscs, and fluorinated surfactants: three nonconventional approaches to studying membrane proteins in aqueous solutions. *Annu Rev Biochem*, 2010. **79**: p. 737-775.
- [5] D.E. Warschawski, et al., Choosing membrane mimetics for NMR structural studies of transmembrane proteins. *Biochim Biophys Acta*, 2011. **1808**(8): p. 1957-1974.

- [6] A.M. Seddon, P. Curnow, and P.J. Booth, Membrane proteins, lipids and detergents: not just a soap opera. *Biochim Biophys Acta*, 2004. **1666**(1-2): p. 105-117.
- [7] T.H. Bayburt, Y.V. Grinkova, and S.G. Sligar, Assembly of single bacteriorhodopsin trimers in bilayer nanodiscs. *Arch Biochem Biophys*, 2006. **450**(2): p. 215-222.
- [8] I.G. Denisov, et al., Directed self-assembly of monodisperse phospholipid bilayer Nanodiscs with controlled size. *J Am Chem Soc*, 2004. **126**(11): p. 3477-3487.
- [9] A. Viegas, T. Viennet, and M. Etzkorn, The power, pitfalls and potential of the nanodisc system for NMR-based studies. *Biol Chem*, 2016. **397**(12): p. 1335-1354.
- [10] T.H. Bayburt, J.W. Carlson, and S.G. Sligar, Reconstitution and imaging of a membrane protein in a nanometer-size phospholipid bilayer. *J Struct Biol*, 1998. **123**(1): p. 37-44.
- [11] T.H. Bayburt, and S.G. Sligar, Single-molecule height measurements on microsomal cytochrome P450 in nanometer-scale phospholipid bilayer disks. *Proc Natl Acad Sci U S A*, 2002. **99**(10): p. 6725-6730.
- [12] J. Borch, and T. Hamann, The nanodisc: a novel tool for membrane protein studies. *Biol Chem*, 2009. **390**(8): p. 805-814.
- [13] B.A. Chromy, et al., Different apolipoproteins impact nanolipoprotein particle formation. *J Am Chem Soc*, 2007. **129**(46): p. 14348-14354.
- [14] T.H. Bayburt, and S.G. Sligar, *Membrane protein assembly into Nanodiscs*. *FEBS Lett*, 2010. **584**(9): p. 1721-1727.
- [15] Y.V. Grinkova, I.G. Denisov, and S.G. Sligar, Engineering extended membrane scaffold proteins for self-assembly of soluble nanoscale lipid bilayers. *Protein Eng Des Sel*, 2010. **23**(11): p. 843-848.
- [16] X.M. Wang, et al., Smaller Nanodiscs are Suitable for Studying Protein Lipid Interactions by Solution NMR. *Protein Journal*, 2015. **34**(3): p. 205-211.
- [17] Z. Zhang, et al., Ca²⁺ modulating alpha-synuclein membrane transient interactions revealed by solution NMR spectroscopy. *Biochim Biophys Acta*, 2014. **1838**(3): p. 853-858.
- [18] A.J. Leitz, et al., Functional reconstitution of Beta2-adrenergic receptors utilizing self-assembling Nanodisc technology. *Biotechniques*, 2006. **40**(5): p. 601-612.
- [19] F. Hagn, et al., Optimized phospholipid bilayer nanodiscs facilitate high-resolution structure determination of membrane proteins. *J Am Chem Soc*, 2013. **135**(5): p. 1919-1925.
- [20] R. Puthenveetil, and O. Vinogradova, Optimization of the design and preparation of nanoscale phospholipid bilayers for its application to solution NMR. *Proteins*, 2013. **81**(7): p. 1222-1231.
- [21] M.L. Nasr, et al., Covalently circularized nanodiscs for studying membrane proteins and viral entry. *Nat Methods*, 2017. **14**(1): p. 49-52.

- [22] B.H. Justesen, et al., Isolation of monodisperse nanodisc-reconstituted membrane proteins using free flow electrophoresis. *Anal Chem*, 2013. **85**(7): p. 3497-3500.
- [23] M.T. Marty, et al., Bayesian deconvolution of mass and ion mobility spectra: from binary interactions to polydisperse ensembles. *Anal Chem*, 2015. **87**(8): p. 4370-4376.
- [24] M.T. Marty, et al., Native mass spectrometry characterization of intact nanodisc lipoprotein complexes. *Anal Chem*, 2012. **84**(21): p. 8957-8960.
- [25] S. Stoilova-McPhie, et al., Lipid nanotechnologies for structural studies of membrane-associated proteins. *Proteins*, 2014. **82**(11): p. 2902-2909.
- [26] A. Kijac, et al., Lipid-protein correlations in nanoscale phospholipid bilayers determined by solid-state nuclear magnetic resonance. *Biochemistry*, 2010. **49**(43): p. 9190-9198.
- [27] J.C. Phillips, et al., Predicting the structure of apolipoprotein A-I in reconstituted high-density lipoprotein disks. *Biophys J*, 1997. **73**(5): p. 2337-2346.
- [28] J.M. Boettcher, et al., Atomic view of calcium-induced clustering of phosphatidylserine in mixed lipid bilayers. *Biochemistry*, 2011. **50**(12): p. 2264-2273.
- [29] Z.O. Shenkarev, et al., Lipid-protein nanodiscs: possible application in high-resolution NMR investigations of membrane proteins and membrane-active peptides. *Biochemistry (Mosc)*, 2009. **74**(7): p. 756-765.
- [30] S.G. Rasmussen, et al., Structure of a nanobody-stabilized active state of the beta(2) adrenoceptor. *Nature*, 2011. **469**(7329): p. 175-180.
- [31] D.M. Rosenbaum, et al., Structure and function of an irreversible agonist-beta(2) adrenoceptor complex. *Nature*, 2011. **469**(7329): p. 236-240.
- [32] B.T. DeVree, et al., Allosteric coupling from G protein to the agonist-binding pocket in GPCRs. *Nature*, 2016. **535**(7610): p. 182-186.
- [33] Y. Gao, et al., TRPV1 structures in nanodiscs reveal mechanisms of ligand and lipid action. *Nature*, 2016. **534**(7607): p. 347-351.
- [34] C. Gatsogiannis, et al., Membrane insertion of a Tc toxin in near-atomic detail. *Nat Struct Mol Biol*, 2016. **23**(10): p. 884-890.
- [35] W. Mi, et al., Structural basis of MsbA-mediated lipopolysaccharide transport. *Nature*, 2017. **549**(7671): p. 233-237.
- [36] F. Hagn, and G. Wagner, Structure refinement and membrane positioning of selectively labeled OmpX in phospholipid nanodiscs. *J Biomol NMR*, 2015. **61**(3-4): p. 249-260.
- [37] L. Morgado, et al., Characterization of the insertase BamA in three different membrane mimetics by solution NMR spectroscopy. *J Biomol NMR*, 2015. **61**(3-4): p. 333-345.
- [38] M. Casiraghi, et al., Functional Modulation of a G Protein-Coupled Receptor Conformational Landscape in a Lipid Bilayer. *J Am Chem Soc*, 2016. **138**(35): p. 11170-11175.
- [39] J.L. Baylon, et al., Characterizing the membrane-bound state of cytochrome P450 3A4: structure, depth of insertion, and orientation. *J Am Chem Soc*, 2013. **135**(23): p. 8542-8551.

- [40] J. Heuveling, et al., Conformational changes of the bacterial type I ATP-binding cassette importer HisQMP2 at distinct steps of the catalytic cycle. *Biochim Biophys Acta*, 2014. **1838**(1 Pt B): p. 106-116.
- [41] F. Finkenwirth, et al., ATP-dependent Conformational Changes Trigger Substrate Capture and Release by an ECF-type Biotin Transporter. *J Biol Chem*, 2015. **290**(27): p. 16929-16942.
- [42] C. Martens, et al., Lipids modulate the conformational dynamics of a secondary multidrug transporter. *Nat Struct Mol Biol*, 2016. **23**(8): p. 744-751.
- [43] F.J. Alvarez, C. Orelle, and A.L. Davidson, Functional reconstitution of an ABC transporter in nanodiscs for use in electron paramagnetic resonance spectroscopy. *J Am Chem Soc*, 2010. **132**(28): p. 9513-9515.
- [44] F.J. Alvarez, et al., Full engagement of liganded maltose-binding protein stabilizes a semi-open ATP-binding cassette dimer in the maltose transporter. *Mol Microbiol*, 2015. **98**(5): p. 878-894.
- [45] D.R. McDougle, et al., Incorporation of charged residues in the CYP2J2 F-G loop disrupts CYP2J2-lipid bilayer interactions. *Biochim Biophys Acta*, 2015. **1848**(10 Pt A): p. 2460-2470.
- [46] I.G. Denisov, and S.G. Sligar, Nanodiscs for structural and functional studies of membrane proteins. *Nat Struct Mol Biol*, 2016. **23**(6): p. 481-486.
- [47] A. Luthra, et al., Nanodiscs in the studies of membrane-bound cytochrome P450 enzymes. *Methods Mol Biol*, 2013. **987**: p. 115-127.
- [48] M. Gregory, et al., Differential hydrogen bonding in human CYP17 dictates hydroxylation versus lyase chemistry. *Angew Chem Int Ed Engl*, 2013. **52**(20): p. 5342-5345.
- [49] P.J. Mak, et al., Unveiling the crucial intermediates in androgen production. *Proc Natl Acad Sci U S A*, 2015. **112**(52): p. 15856-15861.
- [50] P.J. Mak, et al., Resonance Raman spectroscopy reveals that substrate structure selectively impacts the heme-bound diatomic ligands of CYP17. *Biochemistry*, 2014. **53**(1): p. 90-100.
- [51] P.J. Mak, et al., Resonance Raman spectroscopy of the oxygenated intermediates of human CYP19A1 implicates a compound i intermediate in the final lyase step. *J Am Chem Soc*, 2014. **136**(13): p. 4825-4828.
- [52] I.G. Denisov, and S.G. Sligar, Cytochromes P450 in nanodiscs. *Biochim Biophys Acta*, 2011. **1814**(1): p. 223-229.
- [53] A. Luthra, I.G. Denisov, and S.G. Sligar, Temperature derivative spectroscopy to monitor the autoxidation decay of cytochromes P450. *Anal Chem*, 2011. **83**(13): p. 5394-5399.
- [54] H. Tsukamoto, and D.L. Farrens, A constitutively activating mutation alters the dynamics and energetics of a key conformational change in a ligand-free G protein-coupled receptor. *J Biol Chem*, 2013. **288**(39): p. 28207-28216.

- [55] L. Xu, et al., Protonation Dynamics on Lipid Nanodiscs: Influence of the Membrane Surface Area and External Buffers. *Biophys J*, 2016. **110**(9): p. 1993-2003.
- [56] T.H. Bayburt, et al., Transducin activation by nanoscale lipid bilayers containing one and two rhodopsins. *J Biol Chem*, 2007. **282**(20): p. 14875-14881.
- [57] S. Maric, et al., Biosynthetic preparation of selectively deuterated phosphatidylcholine in genetically modified *Escherichia coli*. *Appl Microbiol Biotechnol*, 2015. **99**(1): p. 241-254.
- [58] B.J. Baas, I.G. Denisov, and S.G. Sligar, Homotropic cooperativity of monomeric cytochrome P450 3A4 in a nanoscale native bilayer environment. *Arch Biochem Biophys*, 2004. **430**(2): p. 218-228.
- [59] I. Kucharska, et al., Optimizing nanodiscs and bicelles for solution NMR studies of two beta-barrel membrane proteins. *J Biomol NMR*, 2015. **61**(3-4): p. 261-274.
- [60] T.K. Ritchie, et al., Chapter 11 - Reconstitution of membrane proteins in phospholipid bilayer nanodiscs. *Methods Enzymol*, 2009. **464**: p. 211-231.
- [61] M. Zhang, et al., Reconstitution of the Cytb5-CytP450 Complex in Nanodiscs for Structural Studies using NMR Spectroscopy. *Angew Chem Int Ed Engl*, 2016. **55**(14): p. 4497-4499.
- [62] A. Shaw, et al., The local phospholipid environment modulates the activation of blood clotting. *J Biol Chem*, 2007. **282**: p. 6556-6563.
- [63] T. Kawai, et al., Catalytic activity of MsbA reconstituted in nanodisc particles is modulated by remote interactions with the bilayer. *FEBS Lett*, 2011. **585**(22): p. 3533-3537.
- [64] C. Roos, et al., Characterization of co-translationally formed nanodisc complexes with small multidrug transporters, proteorhodopsin and with the *E. coli* MraY translocase. *Biochim Biophys Acta*, 2012. **1818**(12): p. 3098-3106.
- [65] L. Shi, et al., SNARE proteins: one to fuse and three to keep the nascent fusion pore open. *Science*, 2012. **335**(6074): p. 1355-1359.
- [66] H. Bao, et al., Exocytotic fusion pores are composed of both lipids and proteins. *Nat Struct Mol Biol*, 2016. **23**(1): p. 67-73.
- [67] R.B. Rues, V. Dotsch, and F. Bernhard, Co-translational formation and pharmacological characterization of beta1-adrenergic receptor/nanodisc complexes with different lipid environments. *Biochim Biophys Acta*, 2016. **1858**(6): p. 1306-1316.
- [68] K. Dalal, et al., Structure, binding, and activity of Syd, a SecY-interacting protein. *J Biol Chem*, 2009. **284**(12): p. 7897-7902.
- [69] M.D. Hartley, P.E. Schneggenburger, and B. Imperiali, Lipid bilayer nanodisc platform for investigating polyprenol-dependent enzyme interactions and activities. *Proc Natl Acad Sci U S A*, 2013. **110**(52): p. 20863-20870.
- [70] J. Borch, et al., Nanodiscs for immobilization of lipid bilayers and membrane receptors: kinetic analysis of cholera toxin binding to a glycolipid receptor. *Anal Chem*, 2008. **80**(16): p. 6245-6252.

- [71] A.C. Leney, et al., Nanodiscs and electrospray ionization mass spectrometry: a tool for screening glycolipids against proteins. *Anal Chem*, 2014. **86**(11): p. 5271-5277.
- [72] J. Roy, et al., Direct Capture of Functional Proteins from Mammalian Plasma Membranes into Nanodiscs. *Biochemistry*, 2015. **54**(41): p. 6299-6302.
- [73] D. Proverbio, et al., Functional properties of cell-free expressed human endothelin A and endothelin B receptors in artificial membrane environments. *Biochim Biophys Acta*, 2013. **1828**(9): p. 2182-2192.
- [74] T.Y. Lee, et al., Tuning the Photocycle Kinetics of Bacteriorhodopsin in Lipid Nanodiscs. *Biophys J*, 2015. **109**(9): p. 1899-1906.
- [75] A.W. Shaw, et al., The local phospholipid environment modulates the activation of blood clotting. *J Biol Chem*, 2007. **282**(9): p. 6556-6563.
- [76] S. Inagaki, R. Ghirlando, and R. Grishammer, Biophysical characterization of membrane proteins in nanodiscs. *Methods*, 2013. **59**(3): p. 287-300.
- [77] T. Boldog, M. Li, and G.L. Hazelbauer, Using Nanodiscs to create water-soluble transmembrane chemoreceptors inserted in lipid bilayers. *Methods Enzymol*, 2007. **423**: p. 317-335.
- [78] H. Tsukamoto, et al., Monomeric rhodopsin is the minimal functional unit required for arrestin binding. *J Mol Biol*, 2010. **399**(3): p. 501-511.
- [79] M. Alami, et al., Nanodiscs unravel the interaction between the SecYEG channel and its cytosolic partner SecA. *EMBO J*, 2007. **26**(8): p. 1995-2004.
- [80] S. Eggenesperger, et al., An annular lipid belt is essential for allosteric coupling and viral inhibition of the antigen translocation complex TAP (transporter associated with antigen processing). *J Biol Chem*, 2014. **289**(48): p. 33098-33108.
- [81] H. Duan, et al., Co-incorporation of heterologously expressed Arabidopsis cytochrome P450 and P450 reductase into soluble nanoscale lipid bilayers. *Arch Biochem Biophys*, 2004. **424**(2): p. 141-153.
- [82] A.W. Shaw, M.A. McLean, and S.G. Sligar, Phospholipid phase transitions in homogeneous nanometer scale bilayer discs. *FEBS Lett*, 2004. **556**(1-3): p. 260-264.
- [83] T.H. Bayburt, and S.G. Sligar, Self-assembly of single integral membrane proteins into soluble nanoscale phospholipid bilayers. *Protein Sci*, 2003. **12**(11): p. 2476-2481.
- [84] A.M. D'Antona, et al., Assembly of an activated rhodopsin-transducin complex in nanoscale lipid bilayers. *Biochemistry*, 2014. **53**(1): p. 127-134.
- [85] D. Ni, et al., Structural and functional analysis of the beta-barrel domain of BamA from *Escherichia coli*. *FASEB J*, 2014. **28**(6): p. 2677-2685.
- [86] M.A. Schuler, I.G. Denisov, and S.G. Sligar, Nanodiscs as a new tool to examine lipid-protein interactions. *Methods Mol Biol*, 2013. **974**: p. 415-433.
- [87] J. Xu, et al., SNX16 Regulates the Recycling of E-Cadherin through a Unique Mechanism of Coordinated Membrane and Cargo Binding. *Structure*, 2017. **25**(8): p. 1251-1263 e5.

- [88] Y. Zhu, et al., Structural and biochemical studies reveal UbiG/Coq3 as a class of novel membrane-binding proteins. *Biochem J*, 2015. **470**(1): p. 105-114.
- [89] A. Jonas, Reconstitution of high-density lipoproteins. *Methods Enzymol*, 1986. **128**: p. 553-582.
- [90] A. Jonas, and R.W. Jung, Fluidity of the lipid phase of bovine serum high density lipoprotein from fluorescence polarization measurements. *Biochem Biophys Res Commun*, 1975. **66**(2): p. 651-657.
- [91] C.E. Matz, and A. Jonas, Micellar complexes of human apolipoprotein A-I with phosphatidylcholines and cholesterol prepared from cholate-lipid dispersions. *J Biol Chem*, 1982. **257**(8): p. 4535-4540.
- [92] M.J. Ranaghan, et al., Green proteorhodopsin reconstituted into nanoscale phospholipid bilayers (nanodiscs) as photoactive monomers. *J Am Chem Soc*, 2011. **133**(45): p. 18318-18327.
- [93] C. Paddock, et al., Residues within a lipid-associated segment of the PECAM-1 cytoplasmic domain are susceptible to inducible, sequential phosphorylation. *Blood*, 2011. **117**(22): p. 6012-6023.
- [94] C. Xu, et al., Regulation of T cell receptor activation by dynamic membrane binding of the CD3epsilon cytoplasmic tyrosine-based motif. *Cell*, 2008. **135**(4): p. 702-713.
- [95] M.R. Whorton, and R. MacKinnon, Crystal structure of the mammalian GIRK2 K⁺ channel and gating regulation by G proteins, PIP2, and sodium. *Cell*, 2011. **147**(1): p. 199-208.
- [96] C. Kim, et al., Basic amino-acid side chains regulate transmembrane integrin signalling. *Nature*, 2011. **481**(7380): p. 209-213.
- [97] X.S. Shi, et al., Ca²⁺ regulates T-cell receptor activation by modulating the charge property of lipids. *Nature*, 2013. **493**(7430): p. 111.
- [98] C. Wan, et al., Insights into the molecular recognition of the granuphilin C2A domain with PI(4,5)P2. *Chem Phys Lipids*, 2015. **186**: p. 61-67.

Index

A

adipogenic differentiation, 192-195
alternative treatment, 211, 217
arabidopsis, 62, 78, 79

B

biomolecular NMR laboratory, 243, 244

C

Caenorhabditis elegans (*C. elegans*), 144, 146
cancer cell, 31, 33, 36
cancer, 210, 211, 218
cell division, 33, 34, 38-40
cell proliferation, 31, 35-37
cell signaling, 85, 89
CH/pi, 402
confinement, 268, 274, 278
crystal quality, 108, 111-114
crystallization optimization, 111
crystallization screening, 111, 114-116

D

development, 144-159
drug delivery systems, 12

E

electromagnetic fields, 101
electrostatics, 408, 413, 414
epidermal growth factor receptor (EGFR), 33
epidermal growth factor receptor, 88

F

fragment-based lead discovery, 259, 260

G

gap junction intercellular communication, 85, 87
gene expression, 92-95
genotoxicity, 83, 84, 99

H

h-bond, 402, 403, 404
high magnetic field, 144
high-resolution, 303-305, 308-309, 311
hyperpolarization, 383

I

immunity, 164
iMQCs, 303, 305-306, 309
in vitro studies, 83-85
in-cell, 268, 269, 278
inhomogeneous magnetic fields, 303
interaction, 415, 423-424, 426
iron oxide nanoparticles, 1, 20

L

LF-MF, 164-174

M

macromolecular crowding, 268, 269, 271
magnetic assembly, 29
magnetic fields, 1
membrane protein, 415, 419-432, 435
microorganism, 61, 62, 72
moderate intensity rotating low frequency magnetic fields (MIR-LF-MF), 210, 211
multimodality, 4, 13, 14

N

nanodiscs, 418, 420-435

NMR methodology, 257
NMR spectroscopy, 303-304, 308, 321
NMR, 375, 376, 381
NMR, 420-421, 423-427
nuclear magnetic resonance (NMR)
 spectroscopy, 268, 269

O

osteoblasts, 62, 66-69
osteoclasts, 62, 69-71
osteocytes, 62, 64, 65

P

protein crystallization, 108-111
protein expression, 83, 84, 95
protein structure and function, 268, 269,
 274
protein, 382, 384, 392
protein-protein interaction, 259
pulmonary MRI, 375, 376

R

reproduction, 144, 145, 151

RNA structure, 251, 252

S

silkworm, 62, 74, 75
simulated microgravity, 112, 113, 127
SQCs, 303, 305, 316
static magnetic field (SMF), 31, 33
static magnetic field, 108
static magnetic field, 61, 62
superconducting magnet, 112, 117, 125

T

theranostics, 1, 4, 12
tumor inhibition, 167

X

xingqiyiqi (activating and tonifying Qi),
 210

Other

¹⁹F magnetic resonance imaging, 373
¹⁹F nuclear magnetic resonance, 356